Journal of Petrology

Journal of Petrology, 2022, Vol. 63, No. 3, 1–24
https://doi.org/10.1093/petrology/egac015
Advance Access Publication Date: 24 February 2022
Original Manuscript

OXFORD

Plumbing System Architecture of Late-Stage Hotspot Volcanoes in Eastern Australia

A.T. TAPU*, T. UBIDE, and P. M. VASCONCELOS

School of Earth and Environmental Sciences, The University of Queensland, Brisbane, QLD 4072, Australia

*Corresponding author. E-mail: a.tapu@uqconnect.edu.au

Received 16 October 2020; Revised 22 February 2022; Accepted 23 February 2022

Abstract

Eastern Australia encompasses the longest track (~2000 km) of age-progressive continental volcanoes on Earth. These so-called 'central volcanoes' are shield volcanoes considered as surficial expressions of Cenozoic mantle plume activity under the northward moving Australian continent. Here, we investigate three central volcanoes located in the southern, younger part of the volcanic track (Ebor, Nandewar, and Canobolas) with the aim of unraveling the plumbing system architecture during waning hotspot activity. We explore the duration of volcanic activity and compare long-term evolution of magmatic processes via $^{40}Ar/^{39}Ar$ geochronology, mineral and groundmass chemistry, mineral-melt thermobarometry, and Rhyolite-MELTS thermodynamic simulations. $^{40}Ar/^{39}Ar$ geochronology on groundmass and mineral separates indicates that Ebor is the oldest of the three volcanoes, with duration of at least ~1 Ma (20.4 ± 0.09 to 19.4 ± 0.07 Ma). Nandewar also lasted ~1 Ma (19.4 ± 0.03 to 18.5 ± 0.03 Ma). The Canobolas volcanic complex was younger and shorter lived at ~0.5 Ma (12.0 ± 0.02 to 11.55 ± 0.05 Ma). Interestingly, all three volcanoes share a repetitive tempo of ~0.1 Ma between eruptions. The volcanoes produced porphyritic to aphyric lavas with basalt to trachyte compositions. The phenocryst assemblage includes plagioclase and K-feldspar, pink and green clinopyroxene, rare olivine, and titanomagnetite. Textural and compositional zoning of phenocrysts reveals successive events of mafic replenishment and magma transport prior to eruption. Dissolution textures in plagioclase, coupled with increasing An and FeO_t and decreasing Ba and Ce from crystal cores to mantles, indicate recharge with mafic, oxidised melt. Increasing Mg# and Cr from clinopyroxene cores to rims also supports primitive magma replenishment. Mineral–melt thermobarometry and Rhyolite–MELTS simulations indicate a main level of magma storage in the three volcanoes in the middle crust (18–25-km depth; ~1100°C), repeatedly replenished by undegassed, primitive melts. Green clinopyroxene cores crystallised in isolated pockets where magmas underwent extensive fractionation at depths of 15 to 30 km and ~800°C. The shallow level plumbing system was volumetrically minor and dominated by crystallisation of low-An plagioclase with large melt inclusions, possibly crystallised from degassed, reduced and evolved magma, as suggested by plagioclase hygrometry and f_{O2} modelling. Our combined geochronological and geochemical approach reveals that the three spatially separated but genetically linked volcanoes had comparable, complex plumbing system architectures. Fractionation and repeated magma rejuvenation were critical processes throughout the lifespans of volcanism, and eruptive tempos were controlled by recurrent mafic influx. The maficity of lavas and their crystal cargo correlate with the volume fraction of phenocrysts, suggesting mafic recharge was a key driver of mush remobilisation and eruption. Other volcanoes active during the late stages of plume activity in eastern Australia share similar textural and geochemical features, suggesting that waning hotspot activity may result in increased complexity in magma transport and storage.

Key words: eastern Australia; intraplate volcanoes; plume volcanism; crystal zoning; plumbing system

INTRODUCTION

Magma plumbing pathways are open systems subject to magma recharge, mixing, and differentiation (Streck, 2008; Giacomoni *et al.,* 2014; Bergantz *et al.,* 2015; Cashman *et al.,* 2017; Ubide & Kamber, 2018; Edmonds *et al.,* 2019). Mineral populations record information about open-system processes while the crystals grow, are injected into different magma reservoirs, and are later transported to the surface. Therefore, temporal variations of mineral textures and chemistries are critical to evaluate changes in magma generation, movement, and differentiation (Newhall, 1979; Pizarro *et al.,* 2019; Costa, 2021; Larrea *et al.,* 2021; Ubide *et al.,* 2021). Mineral-scale investigations are frequently used to study active volcanoes because they help to assess short- to medium-term variations of a volcanic system and possible volcanic hazards (e.g. Stromboli, Ubide *et al.,* 2019b; Di Stefano *et al.,* 2020; Galápagos, Stock *et al.,* 2020; Mt St Helens, Wanke *et al.,* 2019; Mt Etna, Kahl *et al.,* 2011), but this approach is less frequently applied to extinct volcanoes. However, extinct and partially eroded volcanoes allow us to access a comprehensive volcano stratigraphy and explore variations in magma plumbing mechanisms on longer time scales, particularly when mineral chemistry is accompanied by high precision geochronology (Crossingham *et al.,* 2018a, 2018b). Investigating extinct volcanoes in intraplate settings can help better understand the long-term behaviour of active plume-related volcanism.

Eastern Australia hosts the longest age-progressive continental volcanic track on Earth (Fig. 1; Wellman & McDougall, 1974a, 1974b; Johnson, 1989; Davies *et al.,* 2015). Its southward age progression (34–6 Ma; Wellman & McDougall, 1974a; Cohen, 2007; Vasconcelos *et al.,* 2008) is linked to a decrease in eruptive volumes that suggests waning of plume flux with time (Jones & Verdel, 2015). Therefore, the eastern Australia Cenozoic hotspot track provides an exceptional laboratory to investigate magmatic processes, tempos of eruption, and progressive changes in magma plumbing system architecture as a plume wanes. To date, mineral-scale investigations have been applied to a limited number of these volcanic centres (Crossingham *et al.,* 2018a, 2018b). For example, high-resolution geochronology and mineral-scale geochemistry at the Warrumbungles and Comboyne volcanoes, located at the same latitude but 300 km apart, revealed coeval magmatism fed by parallel plumbing systems with similar mantle sources (Crossingham *et al.,* 2018a).

Here, we investigate three volcanoes (Ebor, Nandewar, and Canobolas) emplaced towards the end of the plume-related volcanic activity in eastern Australia (Johnson, 1989), bracketing Warrumbungle and Comboyne volcanoes (Fig. 1). Ebor and Nandewar occur on either side of the Great Dividing Range, while Canobolas is a younger and smaller volcano located west of the Great Dividing Range, postdating the Nandewar and Warrumbungle eruptions (Cohen, 2007; Crossingham *et al.,* 2018b). These volcanoes extruded through areas of similar lithospheric and crustal thickness (Fig. 1; Fishwick *et al.,* 2008; Davies *et al.,* 2015; Ball *et al.,* 2021) but have significantly distinct eruptive volumes (Johnson, 1989) that decrease to the south. We explore durations of volcanism and long-term evolution of plumbing system architecture by combining high-resolution $^{40}Ar/^{39}Ar$ geochronology, petrography, groundmass geochemistry, and mineral chemistry via electron microprobe and laser-ablation ICP-MS mapping. We constrain magma transport and storage conditions preceding eruptions at these spatially separated but genetically linked volcanoes and develop a framework to interpret changes in plumbing system architecture with time in age-progressive volcanic chains.

GEOLOGICAL SETTING

Cenozoic volcanic provinces in east Australia

Cenozoic intraplate volcanoes of eastern Australia are spread along an ~2000-km track and cover a current outcrop area of over 1.6×10^6 km^2 (Wellman, 1971; Wellman & McDougall, 1974a; Johnson, 1989). These volcanoes began to form a discontinuous belt during the opening of the Tasman and Coral Seas (Wellman & McDougall, 1974a; Johnson, 1989). Based on K/Ar ages, volcanic stratigraphy, and geochemistry, Wellman & McDougall (1974a) classified the extensive range of volcanic products into three main groups: central volcanoes, lava fields, and leucitites. Central volcanoes, targeted in this study, are shield volcanoes with a diverse range of eruptive products (bimodal nature, albeit dominantly basaltic) (Wellman & McDougall, 1974a; Johnson, 1989) that show a southward age progression (Fig. 1), younging from 33.6 ± 0.4 Ma at Hillsborough, Queensland, to 6.1 ± 0.5 Ma at Macedon, Victoria (Wellman & McDougall, 1974a).

Central volcanoes have been attributed to plume-derived magmatism as the Australian plate moved northward at an average rate of 66 ± 5 km Ma^{-1} over a mantle plume (Wellman & McDougall, 1974a; Wellman & McDougall, 1974b). A plume origin has been supported by high-resolution $^{40}Ar/^{39}Ar$ geochronology confirming the age-progressive nature of central volcanoes (Cohen, 2002; Waltenberg, 2006; Cohen, 2007, Cohen *et al.,* 2008; Knesel *et al.,* 2008; Vasconcelos *et al.,* 2008; Cohen *et al.,* 2013; Jones, 2018; Crossingham *et al.,* 2018a, 2018b) and geochemical data revealing enrichment in incompatible trace elements and EM-1-type Sr-Nd-Pb isotope signatures (Ewart *et al.,* 1988; Ewart, 1989; Johnson, 1989). While Sutherland *et al.* (2012) proposed multiple continental plume tracks based on plate motion vectors and geochronology, Davies *et al.* (2015) combined geophysical and geochemical evidence to link all onshore central volcanoes into a single ~2000-km long plume track. Interestingly, eruptive volumes decrease from north to south, suggesting hotspot activity waned with time (Jones & Verdel, 2015). Recent thermal modelling of the upper mantle supports a decrease in thermal plume flux through the Cenozoic (Ball *et al.,* 2021).

To test the impact of distinct plume settings on magma transport and storage, Crossingham *et al.* (2018a) investigated coeval central volcanoes (Warrumbungle and Comboyne) sitting ~300 km apart, combining high-resolution $^{40}Ar/^{39}Ar$ geochronology and geochemistry. Despite the geographical distance and separation by the Great Dividing Range, these authors found that the volcanoes developed parallel and analogous plumbing systems, where fractionation and periodic mush replenishments by mafic magma triggered recurrent eruptions throughout the lifetime of both volcanoes. Here, we further test the temporal evolution and eruptive stages of the southern segment of east Australian age-progressive volcanoes by investigating the magma plumbing system of Ebor, Nandewar, and Canobolas, which bracket Warrumbungle and Comboyne and may track the final stages of plume activity in eastern Australia.

Ebor, Nandewar, and Canobolas volcanoes

Ebor, Nandewar, and Canobolas are central volcanoes located in New South Wales (Wellman & McDougall, 1974a; Fig. 1) and have pre-erosion volumes of 300, 150, and 50 km^3, respectively (Johnson, 1989). The three volcanoes formed during a period of intermediate

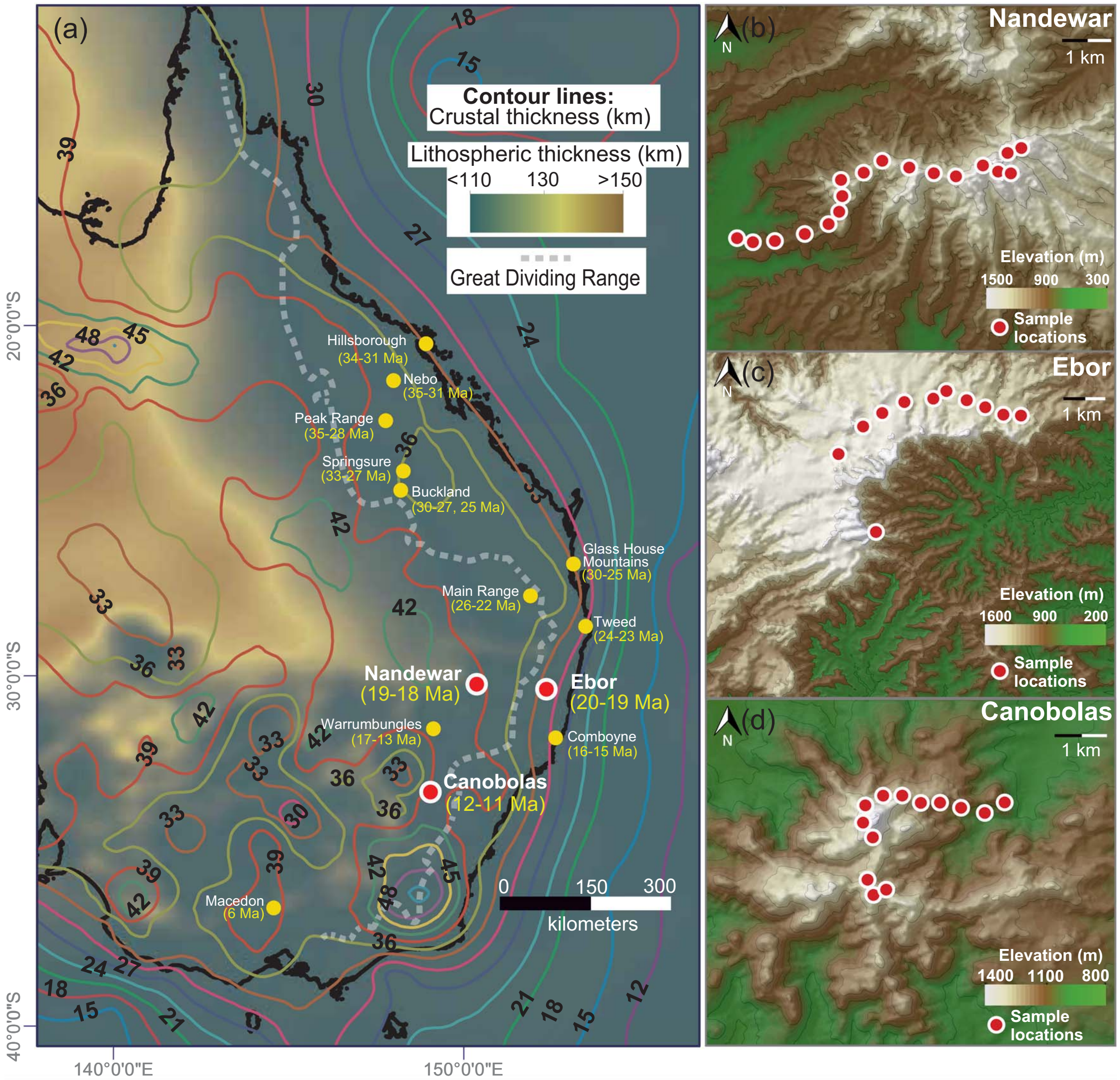

Fig. 1 (a) Map of east Australia including lithospheric thickness (colour shading), crustal thickness (colour contours), and the location and age of central volcanoes. (b–d) Elevation maps and sampling locations (red circles) of Ebor, Nandewar and Canobolas volcanoes. Lithospheric thickness map modified after Davies *et al.* (2015), crustal thickness contour map data from AuSREM (http://rses.anu.edu.au/seismology/AuSREM/index.php), SRTM elevation data from the Intergovernmental Committee on Surveying and Mapping-Elevation and Depth-Foundation Spatial Data (https://elevation.fsdf.org.au). Age data from Cohen (2007); Jones *et al.* (2017, 2020); Jones (2018); Crossingham *et al.* (2018a, 2018b); and references therein.

plate velocity (61 ± 3 km Ma $^{-1}$, Knesel *et al.*, 2008) at the waning stages of hotspot activity (Jones & Verdel, 2015). Ebor and Nandewar are located at the same latitude (30°S), while Canobolas is located close to the end of the age-progressive track at 33°S (Johnson, 1989; Cohen, 2007).

Ebor lavas were dated by ^{40}Ar/^{39}Ar between 19.8 ± 0.7 and 19.25 ± 0.36 Ma (ages from Ashley *et al.*, 1995, recalculated by Cohen, 2007). More recent ^{40}Ar/^{39}Ar ages for Ebor range between 20.0 ± 2 and 19.6 ± 0.2 Ma (Cohen, 2007; Knesel *et al.*, 2008). K/Ar ages from Nandewar volcano range from 21.0 ± 1.0 to 17.4 ± 0.8 Ma (Stipp & McDougall, 1968; Wellman *et al.*, 1969; Wellman & McDougall, 1974a). ^{40}Ar/^{39}Ar geochronology on the upper part of the Nandewar stratigraphy (Cohen, 2007) returned more precise ages of 18.9 ± 0.2 to 18.5 ± 0.2 Ma. K/Ar geochronology from Canobolas by Wellman & McDougall (1974a) yielded ages between 13.0 ± 0.2 and 11.2 ± 0.3 Ma (recalculated by Cohen, 2007). ^{40}Ar/^{39}Ar results yielded similar ages of 13.2 ± 0.3 to 11.6 ± 0.2 Ma (Cohen, 2007; Jones, 2018). However, we note that the ~13 Ma K/Ar and ^{40}Ar/^{39}Ar ages come from the lava flows surrounding the Canobolas volcanic complex, whereas all ages from the volcanic complex itself returned younger ages of 11.9 to 11.2 Ma (Wellman & McDougall, 1974a; Cohen, 2007).

Lavas from Ebor are hawaiites, mugearites, basanites, trachytes, and rhyolites (Ashley *et al.*, 1995). Nandewar is composed of hawaiites, K-hawaiites, and K-mugearites, but it also includes peralkaline trachytes and rhyolites (Stolz, 1985, 1986). Canobolas comprises similar alkaline to peralkaline mafic lavas, together with trachytes, rhyolites, and minor pyroclastic units (Middlemost, 1981). Bulk rock major and trace element compositions from Nandewar and Canobolas indicate initial eruption of hawaiites and formation of more evolved products through fractional crystallisation and volatile transfer (Middlemost, 1981; Stolz, 1985). Fractional crystallisation was also attributed to the evolution of Ebor (Ashley *et al.*, 1995). Clinopyroxene and feldspar chemistry suggests the development of a

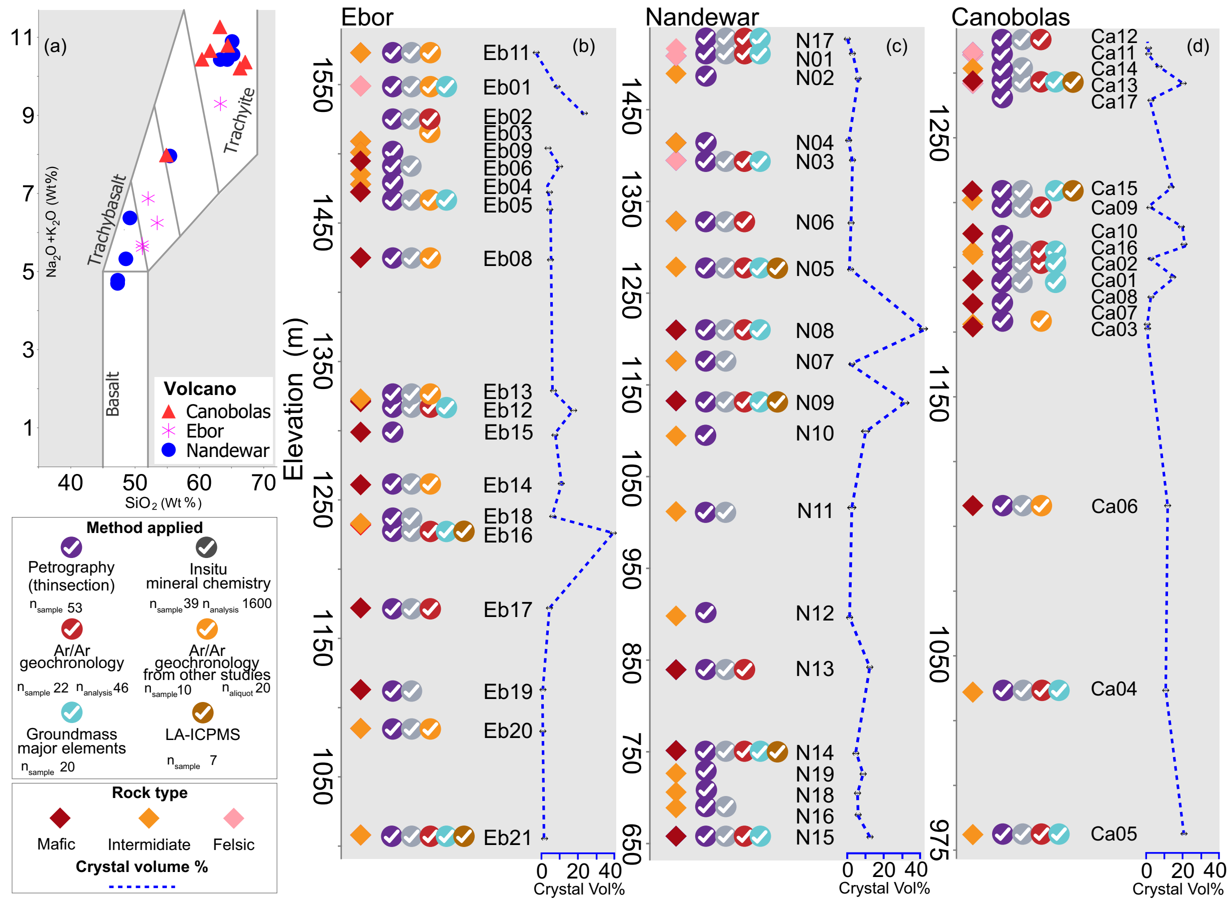

Fig. 2 (a) Major element compositions of groundmass separates from Ebor, Nandewar and Canobolas volcanoes in the total alkalis vs silica diagram (TAS, anhydrous basis; classification fields after Le Bas & Streckeisen, 1991). (b–c–d) Summary of sampling elevations, porphyricity and methods applied to each sample.

thermally and compositionally zoned plumbing system at Canobolas (Middlemost, 1981).

SAMPLES

A total of 53 lava flows varying from basalt to trachyte were sampled from Ebor, Nandewar, and Canobolas volcanoes (Figs 1 and 2). To maximise eruption age coverage, samples were collected across a range of elevations (Fig. 2b–d), particularly where gorges exposed sequences of eruptive products. In Ebor, 18 samples (dominantly mafic, transitioning to intermediate towards the top) were collected from 1000- to 1550-m elevation. In Nandewar, 19 samples were obtained from 650- to 1500-m elevation. This transect covers mafic and intermediate basalts (12 samples) at the base and intermediate to felsic lavas towards the top (seven samples). In Canobolas, the elevation coverage is 975 to 1300 m, with a total of 16 samples. Seven of these are mafic in composition (from 975- to ∼1150-m elevation), and the rest are intermediate and felsic (from 1150- to 1300-m elevation).

The 53 lava samples (18, 19, and 16 from Ebor, Nandewar, and Canobolas, respectively) are petrographically diverse and range among aphyric, sparsely phyric, and porphyritic (Figs 2 and 3), as defined by the abundance of phenocrysts (large crystals >1 mm, typically >3 mm, regardless of their origin). Aphyric lavas (0–5 vol% phenocrysts) are mainly composed of microcrysts <1 mm and variably devitrified glass. In mafic varieties, the microcrysts include plagioclase, olivine, clinopyroxene, and titanomagnetite. Intermediate to felsic varieties are dominated by anorthoclase, sanidine, and titanomagnetite. In addition, the sparsely phyric (5–20 vol% phenocrysts) and porphyritic lavas (>20 vol% phenocrysts) contain phenocrysts that may occur within glomeroporphyritic aggregates (modal assemblages are presented in Supplementary Table 1b; the complete database is available as Electronic Appendix 1, which may be downloaded from http://www.petrology.oupjournals.org/). Phenocrysts include plagioclase, olivine, clinopyroxene, titanomagnetite in mafic rocks, and K-feldspar, clinopyroxene, and minor titanomagnetite in intermediate to felsic rocks. In addition, one of the evolved samples from Ebor contains amphibole. Feldspars form large, elongated phenocrysts and often host melt inclusions (typically <30 μm in size) and/or larger melt pockets (40 to 70 μm in size). Olivine is commonly altered to iddingsite. Clinopyroxene is typically colourless to pink, but green crystals are also present, dominantly in the intermediate to felsic lavas (see section 5.2). Clinopyroxene phenocrysts may contain inclusions of apatite.

ANALYTICAL METHODS

$^{40}Ar/^{39}Ar$ geochronology

A total of 22 mafic, intermediate, and felsic samples (5 from Ebor, 10 from Nandewar, and 7 from Canobolas) were selected to represent

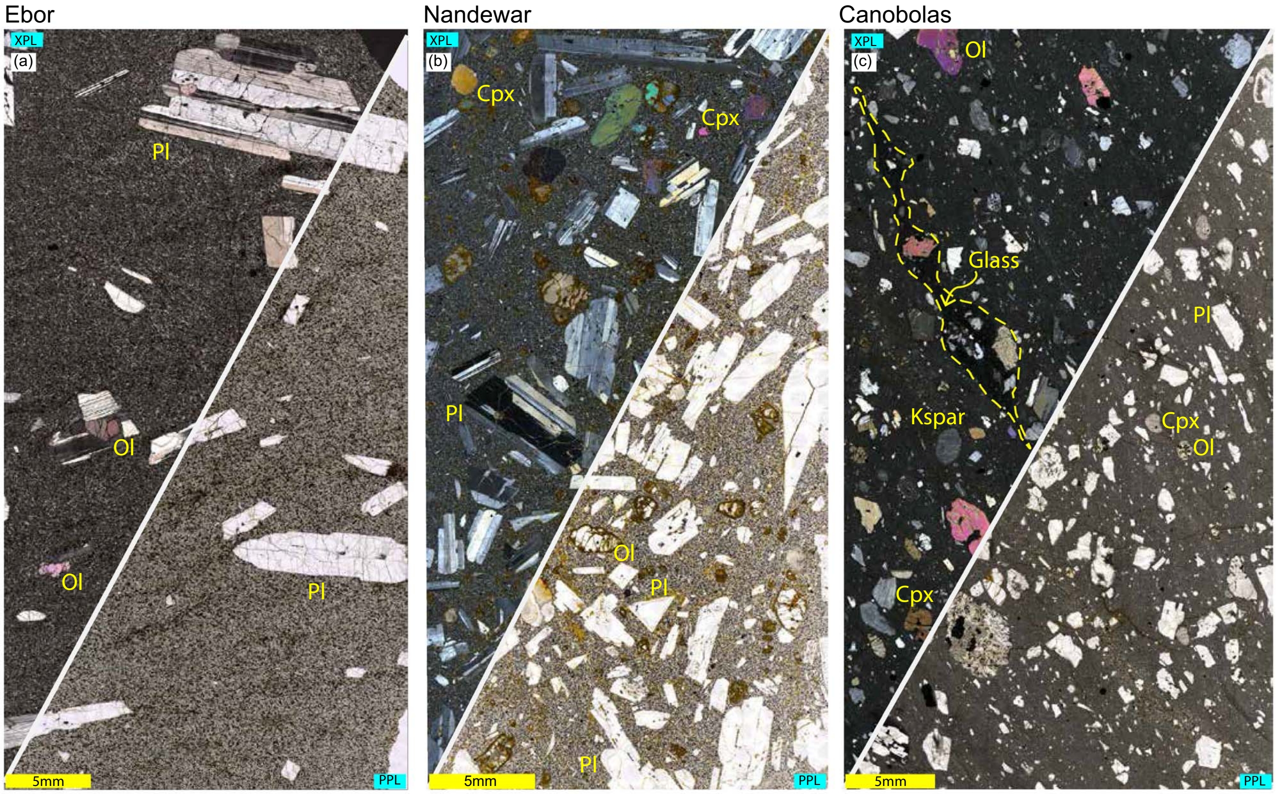

Fig. 3 Petrographic thin section scans in plane-polarised light (PPL; right) and cross-polarised light (XPL; left); (a) sparsely phyric lava from Ebor volcano (Eb15), with plagioclase (Pl) and olivine (Ol) phenocrysts; (b) porphyritic sample from Nandewar volcano (N9), with plagioclase, olivine, clinopyroxene (Cpx) phenocrysts set in a groundmass composed of microcrysts of the same mineral constituents; (c) porphyritic lava from Canobolas volcano (Ca13) with a sliver of glass within the groundmass (yellow dotted area, Kspar - K-feldspar).

the volcano stratigraphy (bottom, middle, and top) and diversity of magmatic products in the three volcanoes and prepared for $^{40}Ar/^{39}Ar$ geochronology. Samples were crushed down to 1–2 mm fragments and acid treated in an ultrasonic bath using 3.5 N HCl and 1 N HNO_3 and repeatedly washed with distilled water, acetone, and ethanol. Fresh groundmass and plagioclase grains (from porphyritic rocks) and whole-rock grains (from fine-grained aphyric rocks) were handpicked and loaded into three 21 pit aluminium discs. In addition, Fish Canyon sanidine (age 28.201 ± 0.046 Ma; Kuiper *et al.*, 2008) was loaded as neutron fluence monitor, and GA 1550 biotite (age 98.560 ± 0.8 Ma; Spell & McDougall, 2003) was loaded as an independent quality monitor. The distribution of samples and standards in aluminium discs followed the arrangement described by Vasconcelos *et al.* (2002). The discs were irradiated for 14 h in a TRIGA-type reactor in the Cd-lined CLCIT facility at the Oregon State University, USA. $^{40}Ar/^{39}Ar$ ages were obtained at the Argon Geochronology Laboratory of the University of Queensland (UQ-AGES, Australia) by incremental heating following Vasconcelos *et al.* (2002). A continuous-wave Ar-ion laser beam (1.8-mm beam diameter) was used to incrementally heat the samples and standard grains. Gas purification was done by a cryocooled trapping system at −130°C and passage of gas through two SAES-50 getter pumps, the first operated at ~450°C and the second at 22°C. After purification, a MAP215-50 mass spectrometer equipped with a third SAES-50 getter pump was used to conduct isotopic analyses. Incremental-heating analysis of two separate aliquots of the same sample was conducted for most samples. One air pipette and three blanks were analysed before and after each sample aliquot.

Data were corrected for atmospheric contamination, mass discrimination, and interferences using the MassSpec software (version 8.132). The $^{40}Ar/^{39}Ar$ value for atmospheric argon of 298.56 ± 0.31 (Lee *et al.*, 2006) was used to calculate mass spectrometer discrimination. The J irradiation factor was calculated by analysing laser total fusion of 15 individual aliquots (1 to 3 grains each) of Fish Canyon sanidine crystals for each disc. The J irradiation factor and all age results are tabulated in Appendix 1.

To crosscheck the $^{40}Ar/^{39}Ar$ analytical procedure, aliquots of GA 1550 biotite standard were irradiated in the same discs and analysed as unknowns. The biotite secondary standard produced near-ideal incremental-heating spectra with ages within the accepted value of 98.56 ± 0.8 Ma (Spell & McDougall, 2003) with initial atmospheric argon values within the accepted range of 298.56 ± 0.8 Ma. The reproducibility of individual results was tested using duplicate analyses. All 22 samples except N17-plagioclase and Eb12-plagioclase were analysed as duplicates, yielding age pairs in agreement within error. In two samples from Nandewar and one sample from Ebor, groundmass separates were complemented with plagioclase separates, which produced results within the statistical uncertainty.

Groundmass major element geochemistry

We analysed the major element composition of 20 stratigraphically and compositionally representative samples (5, 8, and 7 from Ebor, Nandewar, and Canobolas, respectively). Groundmass separates were handpicked, avoiding phenocrysts to ensure geochemical results represent melt chemistry (Magee *et al.*, 2021; Ubide *et al.*, 2022) and powdered in an agate ring and puck mill. Major elements and loss on ignition (LOI) were measured in the Environmental Geochemistry Laboratory at the School of Earth and Environmental Sciences, The University of Queensland.

Groundmass samples were prepared by combining 0.1 g of sample with 0.4 g of lithium metaborate flux in a platinum crucible. The mixture was placed in a Katanax Automatic Fluxer and fused at ~1000°C into a glass bead before being dissolved in 100 ml of 5% nitric acid. Samples, standards, duplicates, and blanks were analysed by inductively coupled optical emission spectrometry (ICP-OES) on a Perkin Elmer Optima system. Standards JG-1a, BHVO-2, SARM2, and SARM 3 were used to monitor accuracy and precision (better than 2% and 6%, respectively; Supplementary Table 1a; the complete database is available as Electronic Appendix 1, which may be downloaded from http://www.petrology.oupjournals.org/).

Mineral chemistry

Major element chemistry: EPMA

In situ major element compositions of phenocrysts, groundmass microcrysts, and glass were determined by electron probe microanalysis (EPMA) on carbon-coated thin sections using a JEOL JXA-8200 at the Centre for Microscopy and Microanalysis (CMM) of The University of Queensland, Australia. We analysed a total of 39 samples (15, 13, and 11 lava flows from Ebor, Nandewar, and Canobolas, respectively, approximately 1300 analyses in total). Samples were selected based on stratigraphy, petrographic diversity, and $^{40}Ar/^{39}Ar$ geochronology results. Analyses were performed using an accelerating voltage of 15 kV, a beam current of 15 nA, and a beam diameter of 2 μm, except for glass, where we used a defocused beam of 10 μm to mitigate volatile loss. The counting times for all elements were 30 s on the peak and ±10 s on each of the two background positions. The matrix correction method was ZAF. For calibration, we used wollastonite (Si-TAP and Ca-PET), orthoclase (K-PET), albite (Na-TAP and Al-TAP), chromite (Fe-LIF and Cr-PET), spessartine garnet (Mn-LIF), F-apatite (P-PET), rutile (Ti-PET), olivine (Mg-TAP), and Ni-olivine (Ni-LIF). In addition, we analysed Springwater olivine, Kakanui augite, Lake Co feldspar, and VG2 glass as secondary standards to monitor precision and accuracy. Precision:Accuracy were typically 2:5% for elements with abundance >10 wt%, 3:7% for elements with abundance of 1–10 wt%, and 5:13% for minor elements <1 wt% (Supplementary Table 2a; the complete database is available as Electronic Appendix 1, which may be downloaded from http://www.petrology.oupjournals.org/). Results were screened using analytical totals and mineral stoichiometry. The filtered dataset includes 1600 analyses (Supplementary Table 1b; the complete database is available as Electronic Appendix 1, which may be downloaded from http://www.petrology.oupjournals.org/).

Trace element chemistry: LA-ICP-MS mapping

Laser ablation inductively coupled plasma mass spectrometry (LA-ICP-MS) mapping was used to investigate trace element compositional zoning in clinopyroxene, plagioclase, and K-feldspar phenocrysts. Seven samples (2, 3, and 2 from Ebor, Nandewar, and Canobolas, respectively; 25 phenocrysts in total) were selected to cover stratigraphic, textural, and compositional variations of the corresponding volcanoes. To directly compare major and trace element compositions, all mapped areas included zones previously analysed by EPMA. We followed the map rastering procedure proposed by Ubide *et al.* (2015). LA-ICP-MS mapping experiments were conducted at The University of Queensland Centre for Geoanalytical Mass Spectrometry, Radiogenic Isotope Facility (UQ RIF-lab, Australia). We used an ASI RESOlution 193-nm excimer UV ArF laser ablation system with a dual-volume Laurin Technic ablation cell and GeoStar Norris software, coupled to a Thermo iCap RQ quadrupole mass spectrometer with Qtegra software. Further details on analytical setup and gas flows are provided in Ubide *et al.* (2019a).

Mapping experiments were performed using a 20-×-20-μm spot size, 20-μm/s translation speed, 10-Hz repetition rate, and 3-J/cm^2 energy fluence. The instrument was tuned and calibrated with ablation lines on NIST612 glass standard reference material. Standards were bracketed before and after individual maps and analysed using the same parameters as the unknowns. NIST612 glass was used as the calibration standard. Accuracy and precision were monitored using BHVO-2G and BCR-2G glasses as secondary standards. Precision:Accuracy were better than 5:10% for all analysed trace elements (Supplementary Table 2b; the complete database is available as Electronic Appendix 1, which may be downloaded from http://www.petrology.oupjournals.org/).

Data reduction was undertaken with Iolite v2.5 software (Paton *et al.*, 2011) in quantitative mode, using major element EPMA data as internal standard: 20.2 ± 1.1 wt% CaO in clinopyroxene ($n_{\text{spot analyses}}$ 378), 54.8 ± 1.34 wt% SiO_2 in plagioclase ($n_{\text{spot analyses}}$ 495), and 60.8 ± 1.73 wt% SiO_2 in K-feldspar ($n_{\text{spot analyses}}$ 212). After visually identifying zoning patterns on elemental maps, the Iolite plugin 'Monocle' (Petrus *et al.*, 2017) was used to extract average quantitative trace element data from individual crystal zones. The regions of interest were drawn as polygons based on observed zoning in Cr, Ti, Al, and Zr in clinopyroxene and Ba, Ca, and Eu in plagioclase and K-feldspar, and avoiding fractures and inclusions. Maps indicating the regions of interest are shown in Supplementary Fig. 1a and b (the complete database is available as Electronic Appendix 1, which may be downloaded from http://www.petrology.oupjournals.org/).

RESULTS

$^{40}Ar/^{39}Ar$ geochronology

$^{40}Ar/^{39}Ar$ results for 22 samples (5 samples from Ebor, 10 from Nandewar, and 7 from Canobolas) are summarised in Table 1. For completeness, we also include $^{40}Ar/^{39}Ar$ data by Jones (2018) (nine groundmass separates and one mineral separate from Ebor) and Cohen (2007) (groundmass separate). $^{40}Ar/^{39}Ar$ diagrams, including new incremental-heating spectra, ideograms, and isochrons, are presented in Supplementary Fig. 2 (the complete database is available as Electronic Appendix 1, which may be downloaded from http://www.petrology.oupjournals.org/), and a selection of representative age results is shown in Fig. 4.

All samples produced plateau ages. The plateaus were defined as three or more contiguous steps, including >50% of the total ^{39}Ar, where the ages for each consecutive step are within 2σ error from the variance-weighted mean (Fleck *et al.*, 1977). The low-temperature steps from some of the samples produced slightly older results, most likely due to minor excess ^{40}Ar. These steps were not included in the age calculation. One sample (Eb12, mineral separate) produced large errors throughout the step-heating spectra due to low radiogenic ^{40}Ar. Due to minor excess Ar in low temperature steps, inverse isochron ages were considered most reliable, with a few exceptions. Plagioclase samples N1 (Nandewar) and Ca12 (Canobolas) did not produce an isochron because the radiogenic ^{40}Ar fraction (~100%) in the early heating steps was very high compared to the atmospheric ^{40}Ar extracted during the middle to high heating steps, where precise

Table 1: $^{40}Ar/^{39}Ar$ geochronology results for Ebor, Nandewar and Canobolas volcanoes (GM - groundmass analysis, Plag - plagioclase analysis)

Sample	Lab no.	Volcano	Location		Material	No. of steps	Plateau age $\pm 2\sigma$ (Ma)[1]	Plateau steps (% ^{39}Ar)	Isochron age[2]	$^{40}Ar/^{36}Ar$ intercept	Probability age $\pm 2\sigma$ (Ma)[3]
			Latitude	Longitude							
Eb2	10 267–01	Ebor	30°29′16.16’S	152°24′36.12″E	GM	11	20.017 ± 0.066	F-K (71)	**20.139 ± 0.075**	277 ± 33	18.505 ± 0.022
	10 267–02					10	20.125 ± 0.064	G-J (72)		MSWD = 1.1 n = 13	MSWD = 1.5 n = 14
EB12	10 275–02	Ebor	30°24′42.96’S	152°20′38.72″E	GM	11	19.830 ± 0.085	F-K (61)	**19.741 ± 0.077**	319 ± 11	19.783 ± 0.060
	10 275–01					11	19.722 ± 0.077	G-K (52)		MSWD = 1.4 n = 9	MSWD = 1.0 n = 9
	10 274–01	Ebor			Plag	10	19.87 ± 0.78	D-J (90)	**19.80 ± 0.88**	285 ± 50 MSWD = 1 n = 8	19.85 ± 0.78 MSWD = 0.65 n = 8
EB16	10 279–01	Ebor	30°21′2.33’S	152°28′4.10″E	GM	9	20.150 ± 0.094	E-I (65)	**20.145 ± 0.100**	301.5 ± 8.4	20.150 ± 0.094
	10 279–02					10	19.80 ± 0.13	D-F (66)		MSWD = 1 n = 6	MSWD = 1 n = 5
EB17	10 280–01	Ebor	30°20′57.34’S	152°28′38.55″E	GM	11	19.546 ± 0.090	B-K (90)	**19.388 ± 0.071**	292.2 ± 7.7	19.349 ± 0.054
	10 280–02					11	19.332 ± 0.064	B-F (92)		MSWD = 1.4 n = 12	MSWD = 1.1 n = 7
Eb21	10 291–01	Ebor	30°22′15.61’S	152°36′15.88″E	GM	11	19.963 ± 0.047	F-J (71)	**19.973 ± 0.044**	306 ± 10	19.981 ± 0.036
	10 291–02					11	20.034 ± 0.067	D-H (75)		MSWD = 1.5 n = 10	MSWD = 1.1 n = 7
N1	10 240–01	Nandewar	30°16′23.50’S	150° 9′51.58″E	GM	11	18.502 ± 0.035	D-K (94)	**18.516 ± 0.021**	298 ± 16	18.505 ± 0.022
	10 240–02					11	18.504 ± 0.039	G-K (78)		MSWD = 1.1 n = 13	MSWD = 1.5 n = 14
	10 238–01				Plag	11	18.622 ± 0.073	D-J (98)	18.659 ± 0.044	−240 ± 110	**18.662 ± 0.066**
	10 238–02						18.52 ± 0.11	G-J (86)		MSWD = 1.3, N = 17	**MSWD = 1.6 n = 8**
N3	10 243–01	Nandewar	30°16′30.89’S	150° 9′25.59″E	GM	11	18.468 ± 0.039	F-K (84)	**18.555 ± 0.029**	312 ± 14	18.554 ± 0.026
	10 243–02					11	18.533 ± 0.046	F-K (78)		MSWD = 1.4 n = 12	MSWD = 1.2 n = 8
	10 241–01				Plag	11	18.522 ± 0.061	A-J (100)	**18.598 ± 0.054**	330 ± 110 MSWD = 1.3 n = 16	18.551 ± 0.050 MSWD = 1.38 n = 16
	10 241–02					11	18.614 ± 0.068	E-H (86)			
N5	10 246–01	Nandewar	30°17′22.34’S	150° 8′55.08″E	GM	11	18.596 ± 0.082	F-K (83)	**18.678 ± 0.056**	326.0 ± 7.0	18.690 ± 0.044
	10 246–02					11	18.760 ± 0.062	G-K (74)		MSWD = 1.5 n = 9	MSWD = 0.37 n = 5
N6	10 244–01	Nandewar	30°17′36.48’S	150° 8′57.73″E	GM	11	18.676 ± 0.059	E-K (86)	**18.697 ± 0.041**	287 ± 28	18.766 ± 0.038
	10 244–02					11	18.764 ± 0.046	E-K (74)		MSWD = 1.4 n = 12	MSWD = 0.42 n = 8
N8	10 248–01	Nandewar	30°17′8.70’S	150° 8′22.55″E	GM	11	19.141 ± 0.082	E-K (96)	**19.089 ± 0.077**	305.5 ± 2.3	19.090 ± 0.073
	10 248–02					11	18.934 ± 0.097	F-K (62)		MSWD = 1.5 n = 15	MSWD = 1.18 n = 11
N9	10 254–01	Nandewar	30°16′40.15’S	150° 7′34.64″E	GM	11	19.116 ± 0.086	F-K (70)	**19.070 ± 0.076**	319.9 ± 3.3 MSWD = 1.3 n = 13	19.003 ± 0.080 MSWD = 1.49, n = 11
N9	10 254–02	Nandewar				11	18.96 ± 0.13	F-K (61)			
N13a	10 253–1	Nandewar	30°16′52.18’S	150° 4′35.10″E	GM	10	19.073 ± 0.058	D-H (81)	**19.006 ± 0.039**	315.5 ± 9.4	19.024 ± 0.037
	10 253–2					11	18.988 ± 0.048	D-K (83)		MSWD = 1.0 n = 15	MSWD = 0.79 n = 12
N14	10 261–01	Nandewar	30°16′47.35’S	150° 4′12.24″E	GM	11	19.107 ± 0.066	C-I (84)	**19.070 ± 0.063**	298.2 ± 6.9	19.068 ± 0.054
	10 261–02					11	19.052 ± 0.067	C-H (82)		MSWD = 1.4 n = 17	MSWD = 1.47 n = 15

(Continued)

Table 1: $^{40}Ar/^{39}Ar$ geochronology results for Ebor, Nandewar and Canobolas volcanoes (GM - groundmass analysis, Plag - plagioclase analysis)

Sample	Lab no.	Volcano	Location		Material	No. of steps	Plateau age $\pm 2\sigma$ (Ma)[1]	Plateau steps (% ^{39}Ar)	Isochron age[2]	$^{40}Ar/^{36}Ar$ intercept	Probability age $\pm 2\sigma$ (Ma)[3]
			Latitude	Longitude							
N15	10 258–01	Nandewar	30°16′20.46’S	150° 3′39.86″E	GM	11	19.414 ± 0.045	F-K (83)	**19.432 ± 0.034**	292.9 ± 7.8	19.428 ± 0.029
	10 258–02					11	19.485 ± 0.068	E-K (56)		MSWD = 1.3 n = 17	MSWD = 0.58 n = 15
N17	10 259–01	Nandewar	30°15′48.29’S	150° 3′14.08″E	GM	11	18.565 ± 0.030	C-K (81)	**18.540 ± 0.025**	314.5 ± 3.1	18.582 ± 0.026
	10 259–02		30°15′48.29’S	150° 3′14.08″E		11	18.583 ± 0.041	E-K (85)		MSWD = 1.3 n = 15	MSWD = 1.73 n = 13
	10 270–01				Plag	11	18.631 ± 0.047	F-K (95)	**18.597 ± 0.060**	313.0 ± 7.1	18.616 ± 0.044
										MSWD = 1.5 n = 10	MSWD = 0.26 n = 5
Ca2	10 282–01	Canobolas	33°20′34.08’S	149° 1′42.46″E	GM	11	11.737 ± 0.027	E-K (74)	**11.735 ± 0.024**	300.3 ± 2.0	11.736 ± 0.021
	10 282–02		33°20′34.08’S	149° 1′42.46″E		11	11.715 ± 0.043	G-K (70)		MSWD = 1.3 n = 15	MSWD = 1.4 n = 10
	10 290–01				Plag	10	11.732 ± 0.035	D-J (100)	11.689 ± 0.040	313 ± 15	**11.739 ± 0.035**
	10 290–02					10	11.69 ± 0.13	D-J (100)		MSWD = 1.1 n = 17	**MSWD = 1 n = 12**
Ca4	10 283–01	Canobolas	33°20′49.43’S	149° 1′5.22″E	GM	11	11.735 ± 0.024	E-K (78)	**11.866 ± 0.040**	334 ± 31	11.728 ± 0.018
	10 283–02					11	11.755 ± 0.046	E-K (85)		MSWD = 1.5 n = 10	MSWD = 1 n = 8
Ca5	10 285–01	Canobolas	33°20′35.75’S	149° 0′46.03″E	GM	11	12.010 ± 0.031	D-H (86)	**12.005 ± 0.023**	307 ± 34	12.009 ± 0.021
	10 285–02					11	12.008 ± 0.033	F-K (71)		MSWD = 1.2 n = 15	MSWD = 1.10 n = 12
Ca9	10 288–01	Canobolas	33°20′15.90’S	148°58′43.55″E	GM	10	11.856 ± 0.034	C-F (89)	**11.851 ± 0.042**	309.7 ± 4.2	11.856 ± 0.037
	10 288–02					10	11.685 ± 0.070	F-K (61)		MSWD = 1.6 n = 13	MSWD = 1.2 n = 6
Ca12	10 296–01	Canobolas	33°20′27.24’S	148°58′38.70″E	Plag	10	11.791 ± 0.073	D-J (100)	n.a.		**11.811 ± 0.047**
	10 296–02					10	11.833 ± 0.058	F-J (96)			**MSWD = 1.6 n = 15**
Ca13b	10 293–02	Canobolas	33°21′42.33’S	148°59′9.49″E	GM	11	11.88 ± 0.13	G-K (68)	**11.60 ± 0.11**	300.8 ± 1.8	11.653 ± 0.089
	10 293–03					11	11.60 ± 0.12	E-K (78)		MSWD = 1 n = 10	MSWD = 1, n = 9
Ca16	10 294–01	Canobolas	33°21′51.50’S	148°59′36.55″E	GM	10	11.880 ± 0.055	D-J (97)	**11.894 ± 0.061**	294 ± 14	11.881 ± 0.052
	10 294–02					11	11.903 ± 0.032	F-K (79)		MSWD = 1.5 n = 12	MSWD = 1.81 n = 11

n.a. Failed to produce valid results (see results section 5.1).

[1]Plateau age is defined as three or more consecutive steps consisting of at least 50% of the total ^{39}Ar released, and the age values overlap and are within 2σ error (Fleck *et al.*, 1977).

[2]The J factor and irradiation corrections are considered in isochron ages without the uncertainty in potassium decay constant. Isochron ages are within 2σ error.

[3]Probability density plots are based on the assumption that a Gaussian distribution occurs for the errors in an age; when each age plotted, the total for each Gaussian curve was considered (Deino and Potts, 1992).

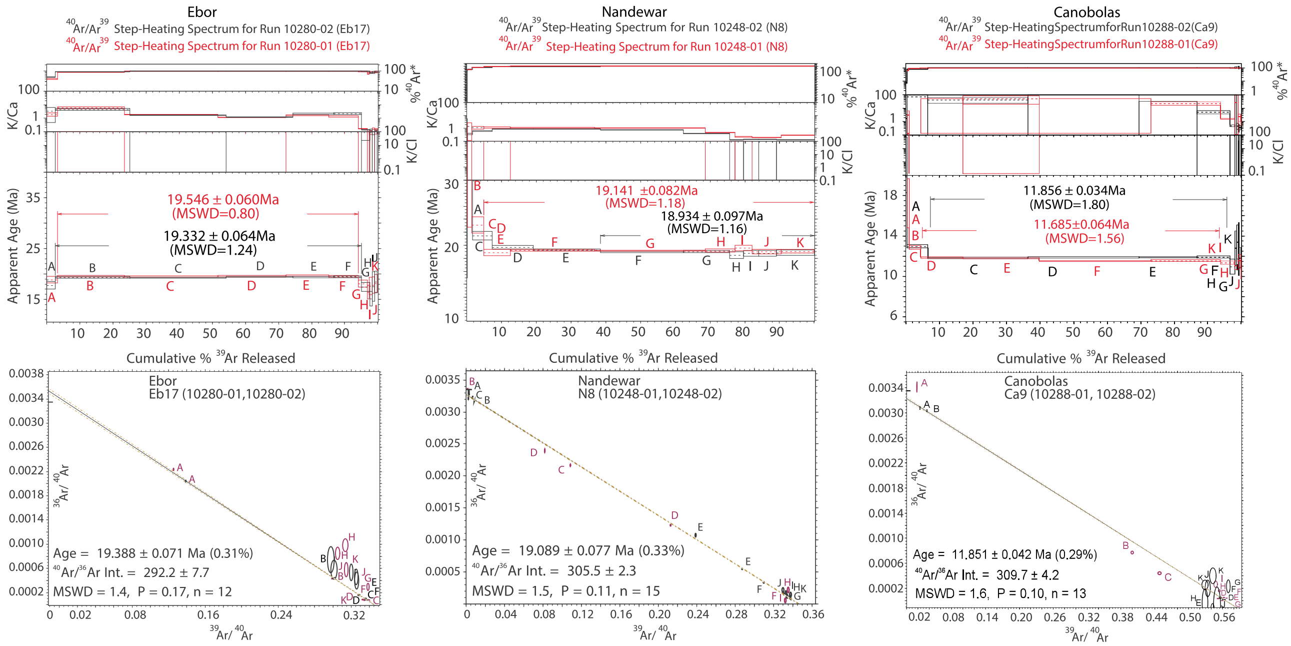

Fig. 4 Representative $^{40}Ar/^{39}Ar$ step-heating spectra and isochron plots for Nandewar, Ebor and Canobolas volcanoes. Note the large, well-defined plateaus and the stark agreement between ages obtained from two different aliquots (duplicate analyses in black and red) from individual samples. Plateau and isochron ages are also coincident. Given the minor excess Ar identified in low-temperature steps, inverse isochron ages were typically preferred over plateau ages as final age results, as they consider the duplicate analyses.

steps cluster at one end of the isochron. Hence, ages estimated from the probability density plots (N1 age, 18.66 ± 0.07 Ma; Ca12 age, 11.81 ± 0.05 Ma) were preferred for these two samples. Nevertheless, the plateau and probability ages are statistically similar. Groundmass and plagioclase separates from individual samples (including Eb12, N1, N3, N17, and Ca2) produced statistically indistinguishable ages. All inverse isochron ages produced atmospheric initial argon values within the error range and included duplicate counterparts of the corresponding groundmass and plagioclase separates, which also yielded statistically identical plateau ages.

Results indicate that eruptive activity at Ebor lasted for ~1.0 Ma. The age of the oldest lava is 20.39 ± 0.09 Ma (sample Eb5; age data from Jones, 2018). Seven lava flows within the lowest- to mid-elevation level yielded an age ranging from 20.4 ± 0.09 to 20.1 ± 0.04 Ma (samples Eb5, Eb13, Eb11, Eb16, Eb2, Eb8, and Eb21). Three intermediate to felsic samples from the uppermost part of the sequence (Eb3 and Eb14 located at the periphery of the volcano from Jones, 2018; plus sample Eb12 from this study) produced an age of ~19.7 ± 0.7 Ma. Lava flow Eb17 (felsic rock collected at the periphery of the volcano) produced the youngest age of 19.39 ± 0.07 Ma for Ebor.

$^{40}Ar/^{39}Ar$ results throughout the stratigraphy of the Nandewar range from 19.43 ± 0.03 to 18.45 ± 0.03 Ma (again, ~1.0 Ma in total). Lava flows from the bottom of the stratigraphy are mafic and yielded an age of 19.43 ± 0.03 Ma (sample N15). There are four flows (N8 19.08 ± 0.08, N9 19.07 ± 0.08, N13a 19.01 ± 0.04, and N14 19.07 ± 0.06) with an age of 19.1 Ma. Sample N9 (isochron age, 19.09 ± 0.08 Ma) indicates minor excess argon ($^{40}Ar/^{36}Ar$ = 319.9 ± 3.3); however, the step-heating and the probability density ages are within statistical uncertainty of the isochron age for all analysed samples.

Intermediate to felsic lava flows from the upper part of the Nandewar stratigraphy have younger ages of 18.7 ± 0.06 to 18.45 ± 0.03 Ma. The youngest flows N1, N3, and N17 (felsic) yielded isochron ages of 18.52 ± 0.02 Ma, 18.56 ± 0.03 Ma, and 18.54 ± 0.03 Ma, respectively, on whole rock separates. The plagioclase separate from sample N3 produced a slightly older isochron age of 18.59 ± 0.05 Ma with a $^{40}Ar/^{36}Ar$ intercept of 330 ± 110. The large error in the $^{40}Ar/^{36}Ar$ intercept possibly originated from the higher amount of radiogenic gas (~100%) and a negligible amount of atmospheric argon, as feldspar separates were free of alteration. Hence, whole rock and plagioclase ages agree within error, but we favour the N3 whole rock result at 18.56 ± 0.03 Ma.

At Canobolas, four lava flows from the lower to the middle part of the sequence (mafic) yielded a very close age range: 12.01 ± 0.02 (Ca5), 11.90 ± 0.06 (Ca16), 11.87 ± 0.04 (Ca4), and 11.85 ± 0.04 Ma (Ca9). Two lava flows from the middle to the top part of the stratigraphy (felsic) produced younger results: 11.74 ± 0.02 (Ca2) and 11.60 ± 0.11 Ma (Ca13). Combining these results with previous $^{40}Ar/^{39}Ar$ data from the volcanic complex (two whole rock ages of 11.65 ± 0.15 Ma, sample Ca6, and 11.55 ± 0.05 Ma, sample Ca3, from Jones, 2018), the volcanic activity of Canobolas ranged from 12.01 ± 0.02 to 11.55 ± 0.05 Ma (~0.5 Ma). We note that there is an ~1 Ma older $^{40}Ar/^{39}Ar$ whole rock age of 13.2 ± 0.3 Ma from lava flows surrounding the volcanic complex (sample BC–171 located ~10 km to the east of the complex; Cohen, 2007). Like Wellman & McDougall (1974a), we conclude that the Canobolas volcanic complex is slightly younger than the lavas surrounding it.

Groundmass geochemistry

Analysed samples are generally unaltered with LOI values of 0.3–1.8 wt% for Ebor, 0.3–2.8 wt% for Nandewar, and 0.3–1.4 wt% for Canobolas (Supplementary Table 1a; the complete database is

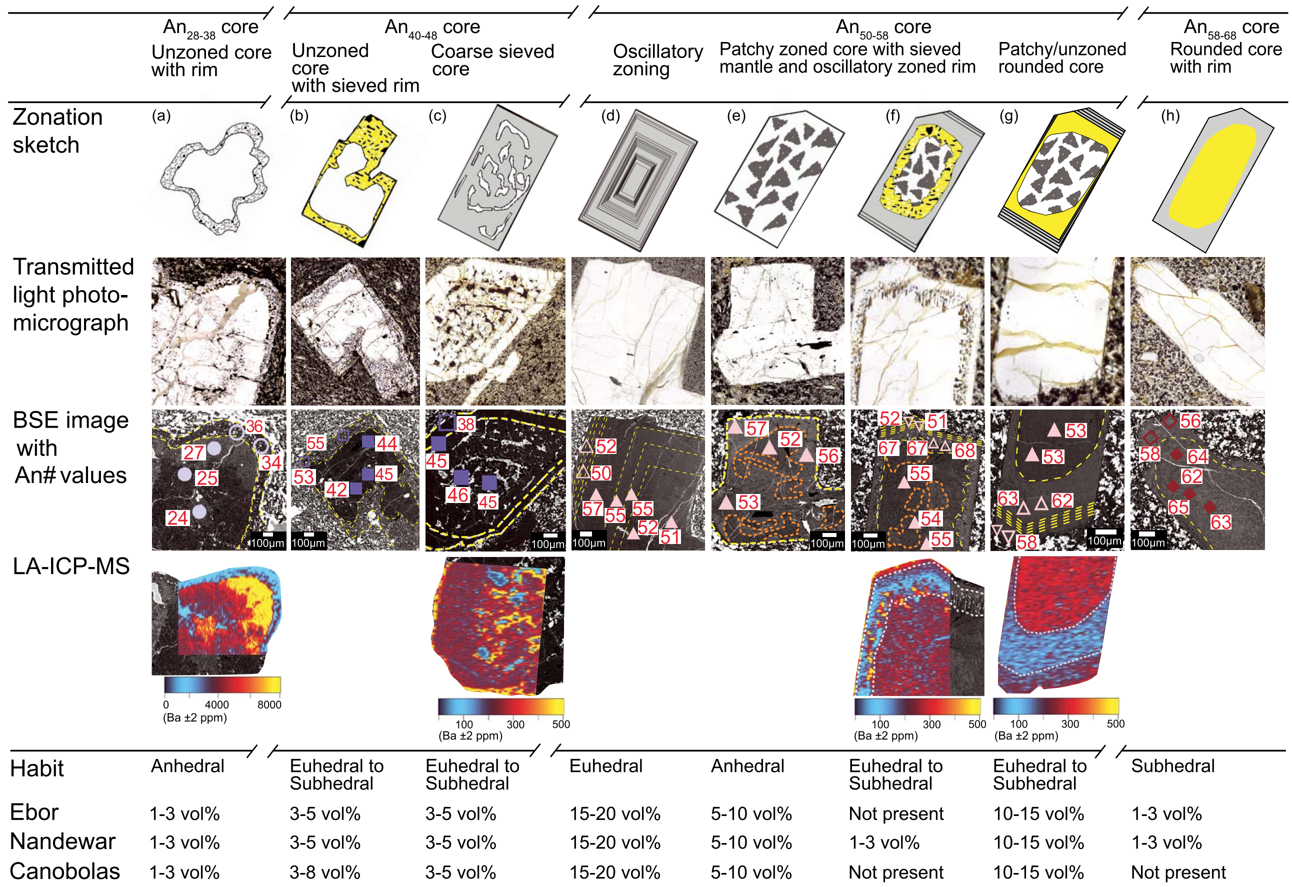

Fig. 5 Textural variations and related major and trace element compositions of plagioclase phenocrysts in the three studied volcanoes. An-anorthite.

available as Electronic Appendix 1, which may be downloaded from http://www.petrology.oupjournals.org/). The lava flows are classified as basalts to trachytes in the total alkalis vs silica diagram (TAS diagram, anhydrous, Fig. 2a; Le Bas & Streckeisen, 1991), defining an alkaline trend. Increasing SiO_2 contents are related to decreasing MgO concentrations from 4.2 to 0.2 wt% MgO. In Ebor, lavas classify as trachybasalts to trachytes, Nandewar lavas range from basalts to trachytes, and Canobolas samples show more evolved compositions, from basaltic trachyandesites to trachytes. Measured groundmass compositions are comparable with previously published compositions for all three volcanoes.

Mineral textures and zoning

Feldspars

Feldspars are the most common phenocryst phase (up to 35 vol% of the rock; Figs. 5 and 6), making up crystals of 3 mm to 2 cm (Fig. 3) with compositions that are primarily plagioclase (andesine to labradorite with $An_{25–68}$) and minor K-feldspar ($Or_{20–50}$). Plagioclase and K-feldspar rarely occur in the same sample as phenocrysts but rather occur in mafic and intermediate-felsic products, respectively (Supplementary Table 1b; the complete database is available as Electronic Appendix 1, which may be downloaded from http://www.petrology.oupjournals.org/). Plagioclase microcrysts (0.2- to 0.8-mm long) are common in the groundmass with compositions of $An_{22–48}$ (oligoclase–andesine). K-feldspar microcrysts (0.1- to 0.7-mm long, $Or_{13–38}$) are only common in the groundmass of lava flows with dominant K-feldspar phenocrysts. Plagioclase and K-feldspar phenocrysts contain melt inclusions; however, inclusions could not be analysed reliably due to their small size (typically <30 μm, and often <20 μm).

Plagioclase

Plagioclase phenocrysts show euhedral to subhedral shapes and complex textures, including oscillatory, patchy, sieved, and rounded, in order of abundance (Fig. 5). Most of the phenocrysts have cores with a compositional range of approximately $An_{50–58}$ (Fig. 6) in all three volcanoes. The cores either are unzoned or show mild variations in anorthite content that link to oscillatory or patchy zonations. Oscillatory zoning is the major textural type (Fig. 5d) and involves low amplitude zones of 5–10 μm and $An_{50–58}$. Patchy zoned cores (Fig. 5e) contain patches of higher ($An_{56\pm0.5}$) and lower ($An_{52\pm0.5}$) anorthite, where high-An infills typically overgrow the low-An patches. Sometimes, the unzoned or patchy cores are rounded and overgrown by an An-rich mantle ($An_{60–70}$) and the An-rich mantle is further outgrown by a slightly An-poor rim ($An_{50–58}$; Fig. 5f–g). The An-rich mantle occasionally shows sieve textures (Fig. 5f). The development of sieve-textured mantles correlates with strong anorthite contrasts between core and mantle zones ($An_{Core} - An_{Mantle} > 10$; Fig. 5b and f).

There are also two groups of cores with lower An contents ($An_{28–38}$ and $An_{40–48}$ cores) in all three volcanoes. The $An_{40–48}$ group includes coarse-sieved textures with large melt inclusions,

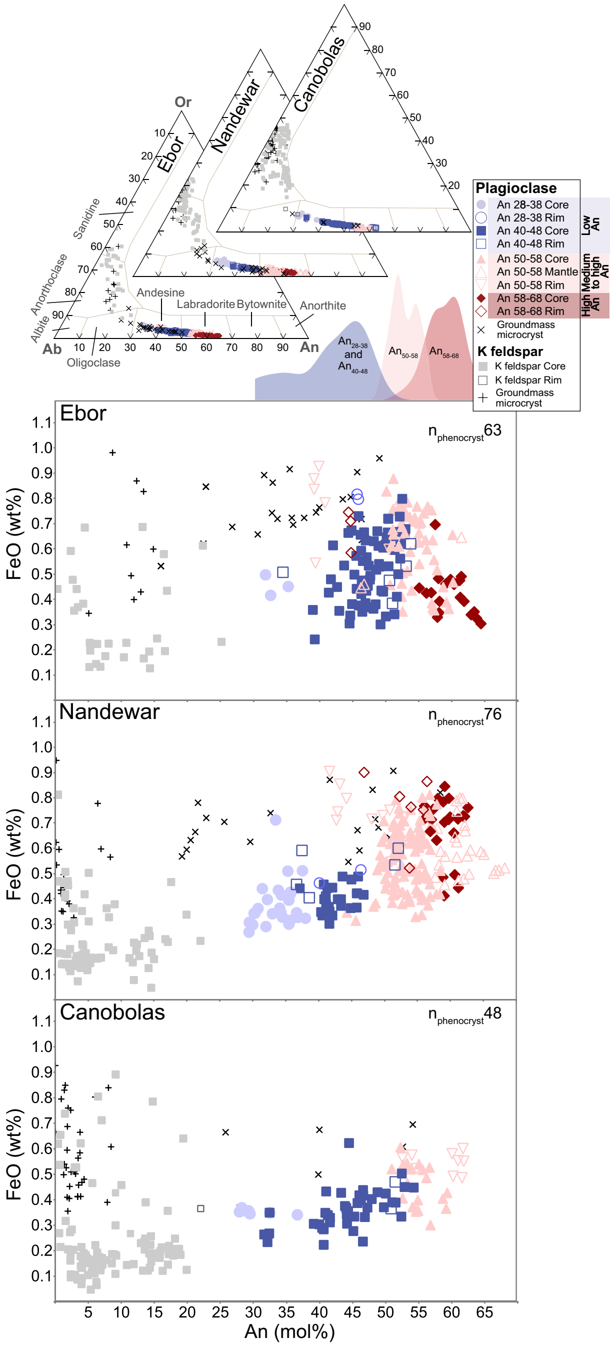

Fig. 6 Classification plots of feldspar (after Deer *et al.*, 1978; Ab-albite, An-anorthite, Or-orthoclase), kernel density estimates of anorthite distribution in plagioclase, and major element variations in feldspar phenocrysts and groundmass microcrysts in Nandewar, Ebor, and Canobolas volcanoes. Analytical uncertainties are smaller than the symbol size. An-anorthite, FeO_t-total iron as FeO.

whereas the $An_{28–38}$ group includes anhedral crystals that lack inclusions (Fig. 5a). Both the $An_{28–38}$ and $An_{40–48}$ cores are occasionally enclosed by An-rich rims ($An_{35–45}$ and $An_{50–58}$, respectively), without intermediate mantles. Those An-rich rims (especially in $An_{40–48}$ cores) are compositionally similar to the mantles surrounding the ubiquitous $An_{50–58}$ cores. However, the rims show stronger sieve textures around $An_{40–48}$ cores (Fig. 5b) than the more general $An_{50–58}$ group. Finally, a group of cores with markedly high anorthite contents ($An_{58–68}$) and rounded edges (Fig. 5h) were found only in Ebor and Nandewar volcanoes. These cores are unzoned, occasionally bounded by lower An rims ($An_{45–55}$) similar to those found around other core types.

In terms of minor elements, FeO_t (total iron as FeO) displays concordant behaviour with An in crystals with $An_{50–58}$ cores in all textural varieties, except for oscillatory zoned crystals, where minor FeO_t variations of 0.4 to 0.6 wt% show non-concordant behaviour. In the rest of the textural varieties, FeO_t increases from cores to An-rich mantles (or An-rich rims) and drops slightly towards An-poor rims ($FeO_{t\ Core:Mantle:Rim}$ 0.4:0.8:0.6 wt%, respectively). Crystals with $An_{40–48}$ (unzoned and patchy varieties) and $An_{28–38}$ cores also exhibit similar concordant behaviour towards An-rich rims ($FeO_{t\ Core:Rim}$ < 0.4:0.6 wt%, respectively). Cores with the highest anorthite contents ($An_{58–68}$) show a different pattern of FeO_t towards the rim, where FeO_t increases slightly with decreasing An, from core to rim ($FeO_{t\ Core:Rim}$ 0.6:0.8 wt%, respectively).

Trace elements are relatively homogeneous within plagioclase zones and show strong variations across zones. Compared to the main $An_{50–58}$ cores (average ± 1σ: Ba_{Core}, 200 ± 2 ppm; Mg_{Core}, 800 ± 3 ppm; Ce_{Core}, 5 ± 0.8 ppm), $An_{60–70}$ mantles are depleted in Ba (<150 ± 2 ppm) and have higher Mg (2000 ± 3 ppm) and Ce (>5 ± 0.8 ppm). The rims are similar to the cores, with slightly higher Ba, Mg, and Ce (Ba_{Rim}, 250 ± 2 ppm; Mg_{Rim}, 1600 ± 3 ppm, $Ce_{Rim.}$ 7.5 ± 0.8 ppm) contents than the cores. $An_{40–48}$ cores have higher Ba (500 ± 2 ppm) than $An_{50–58}$ cores in all textural types. Mg and Ce contents in $An_{40–48}$ cores are 900 ± 3 ppm and 5 ± 0.8 ppm, respectively (similar to $An_{50–58}$ cores). Crystals with $An_{28–38}$ cores display the strongest enrichment in Ba (up to 8000 ± 2 ppm); their rims have average Ba concentrations of 2000 ± 2 ppm (lower than the cores but higher than regular rims). Primitive mantle normalised multi-element patterns (Supplementary Fig. 3a; the complete database is available as Electronic Appendix 1, which may be downloaded from http://www.petrology.oupjournals.org/) are characterised by strong positive anomalies in Ba, Sr, and Eu following their high partitioning in plagioclase. We also observe weak positive anomalies in Ce and Pb and negative anomalies in Sm and Yb.

K-feldspar

K-feldspar is mainly associated with intermediate to felsic lavas found in all three volcanoes. Phenocrysts are mainly anorthoclase and less often sanidine, euhedral to subhedral, and range from 2 to 5 mm in size. The phenocrysts are typically unzoned, but a few examples from Canobolas exhibit plagioclase rims (Fig. 5). Groundmass microcrysts (<0.6 mm size) display similar compositions. The orthoclase component ranges between $Or_{20–50}$ in phenocrysts (with $An_{1–27}$) and $Or_{13–38}$ in microcrysts. K-feldspar phenocrysts have FeO_t concentrations (0.7 to 1.0 wt%) generally higher than plagioclase, and very high Ba concentrations (7000 ± 2 ppm) similar to low-An (An_{30}) plagioclase cores. Two K-feldspar phenocrysts with plagioclase rims ($An_{Core:Rim}$ 15:30) were identified in Canobolas.

Clinopyroxene

Clinopyroxene phenocrysts make up to 3 vol% of porphyritic samples and consist of two types, pink and green, based on colours observed under plane-polarised light (Fig. 7). Pink clinopyroxenes ($Mg\#_{50–82}$; where Mg# = 100 Mg/(Mg + Fe_t), with concentrations expressed on a molar basis and Fe_t representing total iron as Fe^{2+}) are common in mafic lavas (up to ~2 vol% of the rock), with sizes ranging from 1 to 5 mm. Green clinopyroxenes are more Fe-rich

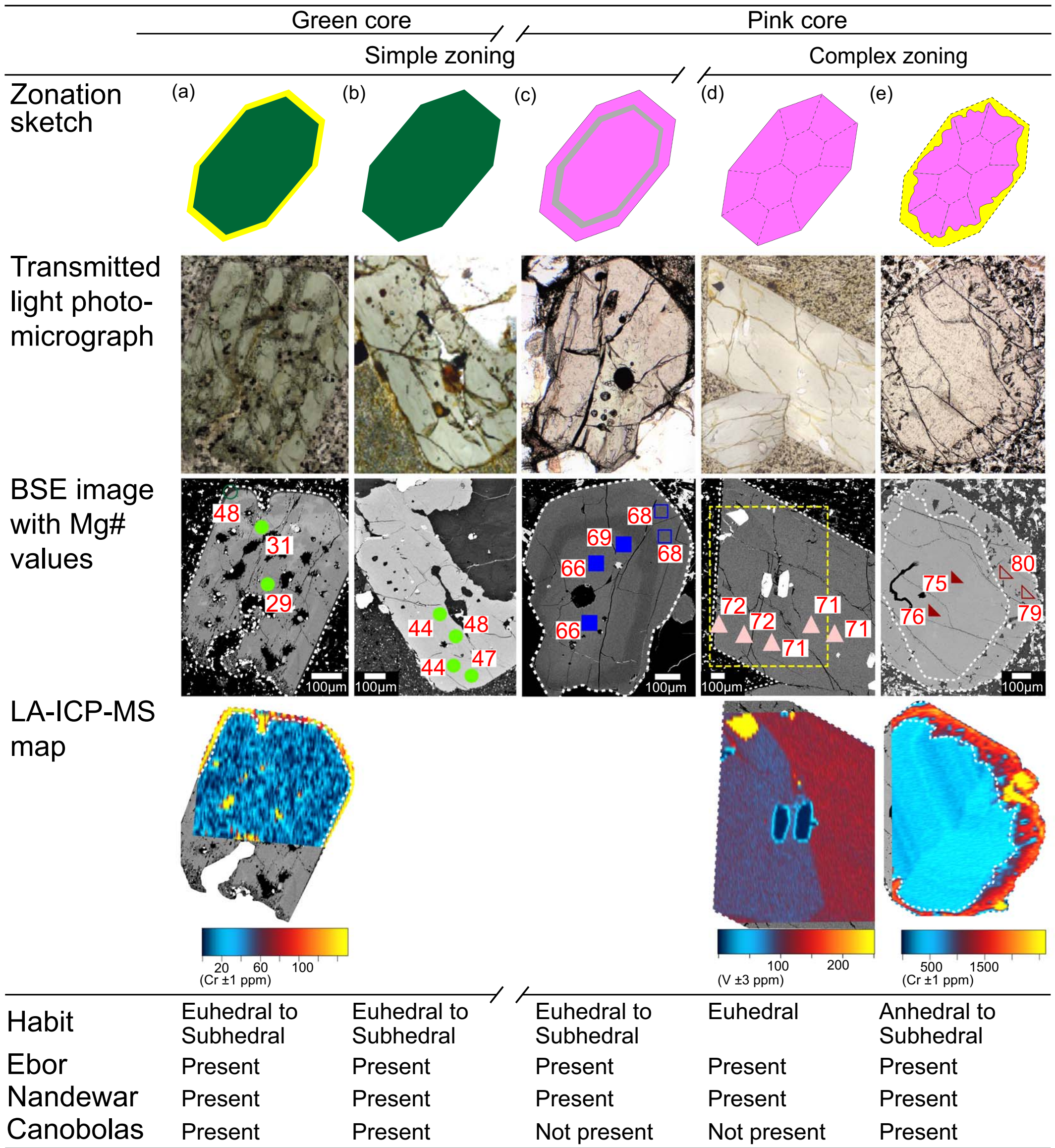

Fig. 7 Textural variations and related major and trace element compositions of clinopyroxene phenocrysts in the three studied volcanoes. Mg#-magnesium number.

($Mg\#_{20–50}$) and often occur in intermediate to felsic lavas (up to 4 mm in size; generally ~1 vol%), mainly associated with K-feldspars. Groundmass microcrysts are almost exclusively pink with a limited compositional range ($Mg\#_{45–60}$).

Pink clinopyroxene

Pink clinopyroxene phenocrysts are subhedral to anhedral augite crystals (Figs 7 and 8). In all three volcanoes, clinopyroxene phenocrysts have cores that often show complex sector zoning and have ~$Mg\#_{70–75}$ compositions (Figs 7 and 8). Sector-zoned cores are occasionally outgrown by higher Mg# rims ($Mg\#_{75–80}$). In Canobolas, a minor group of sector-zoned phenocrysts show lower Mg# (~$Mg\#_{55}$) concentric rims. Simple zoned phenocrysts show normal zoning from homogeneous cores ($Mg\#_{60–65}$) to rims (~$Mg\#_{55}$). On rare occasions (in Canobolas lava flows only), the homogeneous $Mg\#_{60–65}$ cores are overgrown by reversely zoned rims with ~$Mg\#_{68}$.

Sector-zoned cores with $Mg\#_{70–75}$ show distinct trace element zonation patterns (Fig. 7). Al, Ti, V, and Zr partition into prism over hourglass sectors, whereas Cr (<10 ± 0.4 ppm) and Sc (<100 ± 0.2 ppm) are low and relatively constant. The Mg#-rich rims have distinct trace element compositions, especially high concentrations in Cr (Fig. 7e) and other compatible transition metals ($Cr_{Core:Rim}$, 150:>700 ± 0.4 ppm; $Sc_{Core:Rim}$, 50:120 ± 0.2 ppm; $V_{Core:Rim}$, 200: 600 ± 3 ppm, $Ni_{Core:Rim}$ 70:>120 ± 0.2 ppm). Concentrations in rare earth elements and high field strength elements are similar in cores and rims (e.g. $La_{Core:Rim}$, 5:6 ± 0.4 ppm; $Nb_{Core:Rim}$, 2:3 ± 0.2 ppm).

Green clinopyroxene

Green phenocrysts are subhedral to anhedral and texturally unzoned to reversely zoned when surrounded by thin (~5 μm) pink rims (Fig. 7a and b). Green clinopyroxenes classify as ferroaugite (Deer *et al.*, 1978; Fig. 8) and show low Mg# ($Mg\#_{20–50}$). The pink rims

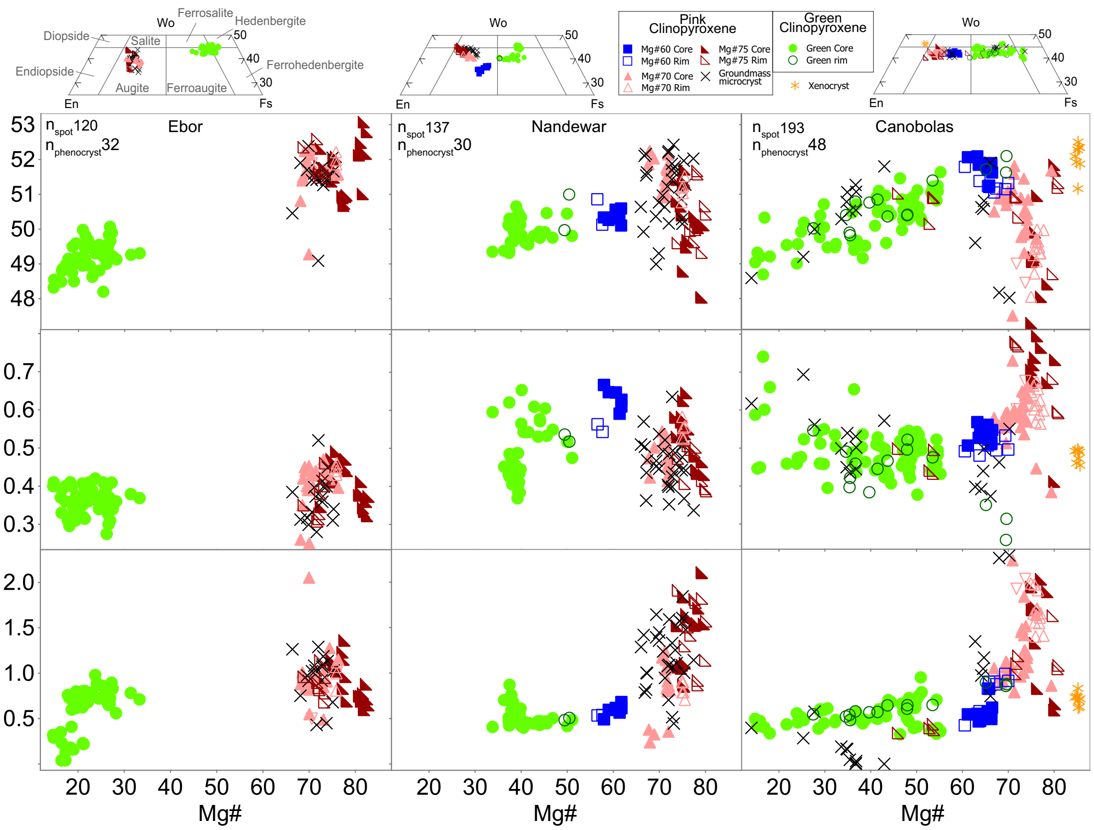

Fig. 8 Clinopyroxene quadrilateral classification plots (after Deer *et al.*, 1978), and major element variations in clinopyroxene phenocrysts and groundmass microcrysts in Nandewar, Ebor, and Canobolas volcanoes. Mg# = 100 Mg/(Mg + Fe_t), where concentrations are expressed on a molar basis, and Fe_t is total iron as Fe^{2+}. Analytical uncertainties are smaller than the symbol size.

have higher Mg# (up to $Mg\#_{70}$, Fig. 8), similar to rims surrounding pink cores.

Green cores have lower concentrations in Cr, V, and Ni (Cr < 20 ± 0.4 ppm, V < 10 ± 3 ppm, Ni < 15 ± 0.2 ppm) with enrichment in Sc (~200 ± 0.2 ppm) and incompatible elements (La, 25 ± 0.4 ppm; Nb, 10 ± 0.2 ppm) relative to pink cores. Pink rims, where present, have higher Cr contents (~100 ppm) than the green cores. Pink and green clinopyroxenes show similar primitive mantle-normalised trace element patterns, with green cores showing stronger negative anomalies in Sr relative to pink cores (Supplementary Fig. 3b; the complete database is available as Electronic Appendix 1, which may be downloaded from http://www.petrology.oupjournals.org/).

Olivine

Subhedral to anhedral olivine phenocrysts are comparatively rare (up to 3 vol% of total rock; 2–6 mm in size; Fig. 3) and only found in mafic lavas. Iddingsite and minor serpentine alteration occur along crystal edges and fractures, and complete iddingsitisation is common. Phenocrysts range typically between approximately Fo_{55} and Fo_{75} (highest Fo_{79}, rare) with normal zoning in all three volcanoes (Supplementary Fig. 4; the complete database is available as Electronic Appendix 1, which may be downloaded from http://www.petrology.oupjournals.org/). Cores are typically Fo_{65} with 0.1–0.2 wt% NiO, 0.3–0.7 wt% MnO, and up to 0.3 wt% CaO, and are overgrown by $Fo_{50–58}$ rims. There is also a high-Fo# core group with Fo_{75} and higher NiO (0.1–0.2 wt%) and lower MnO (0.2–0.3 wt%) and CaO (0.1–0.2 wt%), overgrown by $Fo_{65–70}$ rims. Olivine microcrysts in the groundmass (<0.8 mm in size) have low Fo content (approximately Fo_{55}), with high MnO (0.9 wt%) and CaO (0.3 wt%) compared to the phenocrysts.

Titanomagnetite

Ti-rich magnetite up to 2 mm in size is common in all three volcanoes and is generally associated with olivine, clinopyroxene, and plagioclase phenocrysts and groundmass of the same mineral constituents (Fig. 3). Magnetite as a single phenocryst is rare (<1 vol%). TiO_2 concentrations range from 20 to 30 wt%, both in the inclusions and single phenocrysts. Some of the titanomagnetite phenocrysts have ilmenite rims with TiO_2 ~50 wt%.

DISCUSSION

Ebor, Nandewar, and Canobolas volcanoes share similar durations of volcanic activity, eruptive products, and crystal cargoes, suggesting common volcanic sources, triggers, and intricate magmatic processes before eruption. Hereafter, we assess variations in crystallisation conditions through time to derive a detailed history of the plumbing system architecture feeding late-stage hotspot volcanism in eastern Australia. We first combine our petrographic and geochemical observations to discuss the origin of plagioclase and clinopyroxene populations, which we then test quantitatively using mineral–melt thermobarometry and hygrometry as well as thermodynamic simulations.

Origin of textural and compositional variations in plagioclase

The dominant plagioclase cores ($An_{50–58}$) often display low amplitude microscale zonations and limited An variations between $An_{50–55}$ (Fig. 5d). Oscillatory zoning is commonly interpreted as slow growth at near-equilibrium conditions (Allègre *et al.,* 1981), due to either minor changes in growth kinetics or small fluctuations in temperature (Viccaro *et al.,* 2010; Van Gerve *et al.,* 2020). Experimental data indicate that temperature variations of 50°C can induce An oscillations of ~10 mol% (Couch *et al.,* 2001), in agreement with the variations observed in finely oscillatory zoned crystals. Such oscillations are found in large (up to 2 cm) euhedral phenocrysts without major Fe variations, which suggests stable oxidation conditions (supported by the f_{O2} modelling discussed in section 6.4). Therefore, we infer that the dominant $An_{50–58}$ cores reflect crystallisation in a stable magma reservoir, where minor scale convection may have introduced small temperature gradients, as opposed to strong temperature changes related to mafic recharge that would result in crystal dissolution (Blundy & Cashman, 2001; Viccaro *et al.,* 2014).

Patchy zoned crystals may reflect partial dissolution and recrystallisation processes (Van Gerve *et al.,* 2020). The increase in anorthite from An_{52} patches to An_{57} infills (Fig. 5e) may reflect increasing P_{H2O} due to decompression of volatile-undersaturated magma (Nelson & Montana, 1992; Blundy & Cashman, 2001; Waters & Lange, 2016; Bennett *et al.,* 2019) or recharge with primitive-undegassed melt (Nakamura & Shimakita, 1998). The two processes are not mutually exclusive because mafic recharge could also enhance magma ascent between deep reservoirs (Viccaro *et al.,* 2010, 2014).

Some of the patchy cores ($An_{50–58}$, Fig. 5e and f) are rounded and enclosed by reversely zoned sieved mantles ($An_{65–68}$) and fine oscillatory rims that define normal zoning (~An_{55}). More rarely, the sieved mantles overgrow unzoned but still rounded cores (Fig. 5g). Sieve textures are experimentally reproduced by dissolution and reprecipitation of plagioclase along melt channels due to interaction with more mafic melts (magma mixing; Tsuchiyama, 1985; Nakamura & Shimakita, 1998; Cashman & Blundy, 2013). Hence, the increase in An in sieve mantles relative to the cores, together with the rounded texture of the cores, suggests dissolution and recrystallisation of plagioclase in response to the arrival of hot mafic magma (Tsuchiyama, 1985; Pearce *et al.,* 1987; Nakamura & Shimakita, 1998; Viccaro *et al.,* 2010; Cashman & Blundy, 2013; Viccaro *et al.,* 2014). The increase in An from cores to sieved mantles is coupled with a decrease in Ba and Ce, supporting crystallisation from a more primitive melt (Cao *et al.,* 2019). The final, minor oscillatory zoned rims (Fig. 5f) can be attributed to near-equilibrium growth and relatively stable magma reservoir conditions, similar to the oscillatory-zoned phenocrysts.

The coarse sieved crystals possibly formed under rapid crystallisation conditions that enabled entrapment of melt pools (Baker, 2008; Viccaro *et al.,* 2014) and, hence, potentially higher degrees of magma undercooling (Viccaro *et al.,* 2010). Lower An ($An_{45–48}$) and FeO_t contents confirm that coarse sieved crystals formed at different conditions compared to the higher An ($An_{50–58}$ and $An_{58–68}$ cores) varieties, most likely from a more evolved and reduced magma with lower volatile content (Viccaro *et al.,* 2010; Crabtree & Lange, 2011). Crystallisation of coarse sieved crystals from evolved melts is further supported by higher Ba and Ce concentrations relative to the high An crystals (Nelson & Montana, 1992; Waters & Lange, 2016; Bennett *et al.,* 2019; Cao *et al.,* 2019). Therefore, we suggest the coarse sieved textures might have formed at shallower levels of the magmatic system, with degassing (H_2O loss) leading to increased magma undercooling (Viccaro *et al.,* 2010; Crabtree & Lange, 2011) and melt reduction, as shown in experimental studies (Kirkpatrick *et al.,* 1979; Lofgren, 1980).

Low-An plagioclase cores ($An_{28–38}$ and $An_{40–48}$) are anhedral and show rims with higher An and strong sieve textures, suggesting incorporation into and partial resorption by more mafic melts. Plagioclase with lowest An contents ($An_{28–38}$ cores) could be linked to crystallisation from significantly evolved melts cognate to the plumbing system or could be interpreted as crustal xenocrysts considering that east Australia central volcanoes have been linked to extensive crustal contamination (Ewart *et al.,* 1977; Ewart & Stevens, 1987; Ewart, 1989). The trace element signature of all analysed plagioclases is similar, suggesting a cognate origin. However, further elemental and/or isotopic data would be required to test the origin of low-An cores. The K-feldspar phenocrysts are euhedral and occur in association with green clinopyroxene in intermediate-felsic lavas, suggesting crystallisation within evolved magma pockets.

Origin of textural and compositional variations in clinopyroxene

Pink clinopyroxene phenocrysts (augite) typically have Mg-rich ($Mg\#_{70–75}$) cores with sector zoning (Fig. 7d and e). Strong Al–Ti enrichment in prism sectors relative to hourglass sectors (Supplementary Fig. 1a–iv, vi–viii; the complete database is available as Electronic Appendix 1, which may be downloaded from http://www.petrology.oupjournals.org/) follows typical sector partitioning in other alkaline systems (Nakamura, 1973; Downes, 1974; Leung, 1974; Kouchi *et al.,* 1983; Ubide *et al.,* 2019a, 2019b; Mollo *et al.,* 2020) and suggests low degrees of undercooling in a dynamic crystallisation regime (Ubide *et al.,* 2019a, 2019b; Di Stefano *et al.,* 2020; Klügel *et al.,* 2020; Masotta *et al.,* 2020; Ubide *et al.,* 2021). The small thermal gradients necessary to generate sector zoning may result from slow magma ascent, convection at the margin of a reservoir, and/or magma mixing (Ubide *et al.,* 2019a, 2019b). Loss of H_2O by decompression or flushing with CO_2-rich fluid released from deeper melts may also increase undercooling, inducing sector zoning (Sparks & Pinkerton, 1978; Klügel *et al.,* 2020).

Pyroxene cores often show very distinct dissolution textures overgrown by rims rich in Mg (~$Mg\#_{80}$), Cr, and other compatible metals (Fig. 7e), which can be linked to the injection of more mafic and hot magma that partially dissolved pre-existing cores (Streck, 2008; Ubide *et al.,* 2019a). Mafic recharge could have also led to the growth of An-rich mantles around plagioclase cores. Considering the occurrence of both sector-zoned clinopyroxene and patchy-zoned plagioclase cores in our samples, we suggest that deep magma ascent might have controlled the development of such cores, later overgrown by Mg-Cr-rich and An-rich compositions upon mafic recharge.

Green Fe-rich clinopyroxenes (ferroaugite) are extensively documented in alkaline systems, and their origin is interpreted as either wall rock debris picked up by ascending magma (crustal xenocrysts), mantle xenocrysts, or crystallisation products of evolved magma via deep-seated polybaric differentiation (Wass, 1979; Duda & Schmincke, 1985; Ubide *et al.,* 2014). In our samples, green clinopyroxene cores (Fig. 7a and b) show lower Mg# ($Mg\#_{20–55}$) and higher incompatible trace element concentrations than the more common pink clinopyroxenes. Both pyroxene types, however, show convex-upward, chondrite-normalised REE patterns, opposite to the analysed trend of mantle xenocrysts from the area (Canobolas volcano, Supplementary Fig. 3b; the complete database is available as Electronic Appendix 1, which may be downloaded from http://www.petrology.oupjournals.org/). Primary igneous textures, such as euhedral shapes (Fig. 7a and b), are common in the green clinopyroxene population. Therefore, we discard the possibility that the green clinopyroxenes represent wall rock debris. Rather, the REE resemblance between pink and green clinopyroxenes suggests a cogenetic origin (Villaseca *et al.,* 2020), with green clinopyroxenes crystallising from more evolved but genetically related melts (Fig. 9e). Indeed, green cores show strong negative anomalies in Sr (Supplementary Fig. 3b) that suggest crystallisation after extensive plagioclase fractionation. Green clinopyroxenes occur together with K-feldspars within glomerocrysts in Canobolas felsic rocks, indicating crystallisation from a common, evolved melt. The green phenocryst population possibly crystallised from extensively fractionated, cold melt pockets located at high-pressure conditions, as observed in other alkaline volcanic and subvolcanic settings (Wass, 1979; Duda & Schmincke, 1985; Ubide *et al.,* 2014; Villaseca *et al.,* 2020). We test and quantify conditions of crystallisation in the following section.

Constraining the intensive parameters of crystallisation environments

Clinopyroxene–melt thermobarometry

To estimate the P–T conditions of clinopyroxene crystallisation, we paired pink and green clinopyroxene compositions with equilibrium melts, approximated via groundmass and glass compositions from the same volcanoes. We considered basalt, trachybasalt, and trachyte groundmass geochemistries and glass electron microprobe analyses from Ebor (Eb12, Eb16, and Eb5—glass), Nandewar (N8, N15, and N1), and Canobolas (Ca4, Ca16, and Ca13).

Two tests were used to assess chemical equilibrium between clinopyroxene and melt compositions (Fig. 9a–e). The Fe–Mg exchange equilibrium range ($Kd_{Fe\text{–}Mg}{}^{cpx\text{–}melt} = 0.28 \pm 0.08$; Putirka, 2008; Fig. 9a–c) was complemented with a comparison between diopside and hedenbergite components observed in the analysed crystals vs those predicted from melt compositions (ΔDiHd test following Putirka *et al.,* 1996, and Mollo *et al.,* 2013). In the second test, equilibrium is achieved when ΔDiHd is close to zero (Mollo & Masotta, 2014) and the observed–predicted values plot within or close to the one-to-one line of the 'DiHd observed' vs 'DiHd predicted' diagram (Fig. 9d). The combined $Kd_{Fe\text{–}Mg}{}^{cpx\text{–}melt}$ and ΔDiHd equilibrium assessment are increasingly applied to provide robust equilibrium constraints in natural clinopyroxene-melt pairs (e.g. Neave *et al.,* 2019; Ubide *et al.,* 2019a; Klügel *et al.,* 2020). Here, only data that passed both the Fe–Mg and ΔDiHd equilibrium tests were used to estimate crystallisation pressure–temperature conditions via clinopyroxene–melt thermobarometry. Many rim compositions (~28% of total clinopyroxene dataset) did not pass equilibrium tests and therefore were deemed unsuitable for the application of thermobarometric calibrations. We applied clinopyroxene–melt thermometry by Putirka *et al.* (1996) (T1, ±27°C uncertainty 1σ) and barometry by Putirka *et al.* (2003) (±170 MPa uncertainty 1σ) to pink and green clinopyroxene cores and rims, paired with their equilibrium melts.

High Mg# pink clinopyroxene cores (Mg#$_{70–75}$) yield pressure and temperature conditions of 710 ± 280 MPa and 1126 ± 24°C (average, ±1σ; Fig. 9f–h). Reverse zoned ~Mg#$_{80}$ rims formed under highest temperature (1160 ± 31°C), whereas low Mg# (Mg#$_{60–65}$) pink cores formed at a lower temperature (986 ± 55°C). Green cores (Mg#$_{20–50}$) crystallised within considerably colder magma pockets (794 ± 44°C) relative to the Mg#$_{70–75}$ cores. Pressure conditions are calculated to have been similar in all cases (Fig. 9f–h; Supplementary Fig. 1d; the complete database is available as Electronic Appendix 1, which may be downloaded from http://www.petrology.oupjournals.org/). In detail, pressure results seem to indicate slight variations between volcanoes; however, such variations are within the error of the calibration (see pressure kernel density estimates for individual volcanoes in Supplementary Fig. 1e; the complete database is available as Electronic Appendix 1, which may be downloaded from http://www.petrology.oupjournals.org/). Estimated pressure conditions correspond to crystallisation depths of 3 to 36 km (average ± 1σ: 17.4 ± 9 km) for both green and pink clinopyroxenes (Fig. 9f–h), using a crustal density of 2.85 g cm^{-3} (Collins *et al.,* 2003).

The distribution of thermobarometry results suggests the development of relatively comparable plumbing systems feeding all three volcanoes. The majority of pressure data cluster at ~500–700 MPa, indicating magma storage concentrated at ~18- to 25-km depth in the middle crust (Fig. 9f–h). Pink clinopyroxenes can occur in glomerocrysts with the main plagioclase population (finely oscillatory zoned An$_{50–58}$ plagioclase), suggesting both minerals formed together in such main storage regions. The green cores formed at depths similar to pink cores, indicating recycling of crystals formed in cold pockets by more primitive melts, similar to other alkaline settings (Duda & Schmincke, 1985; Villaseca *et al.,* 2020). Mafic recharge melts formed Mg–Cr-rich clinopyroxene rims and sieve-textured An-rich plagioclase mantles within similar pressure conditions, as further supported by Rhyolite-MELTS (Gualda *et al.,* 2012; Ghiorso & Gualda, 2015) simulations and plagioclase thermobarometry (Putirka, 2005, 2008) below.

Rhyolite-MELTS simulations

To further constrain the pathways of magma storage and ascent to eruption, we performed fractional crystallisation simulations via Rhyolite-MELTS (v1.2.0) (Gualda *et al.,* 2012; Ghiorso v & Gualda, 2015). We focused on mafic products and calculated the starting melt composition by adding 6 wt% Fo$_{79}$ to the groundmass composition of sample N8 (mafic basalt from Nandewar volcano with the highest Mg#). This sample satisfies $Kd_{Fe\text{–}Mg}$ and DiHd equilibrium conditions with pink clinopyroxene. Our modelled starting composition follows the liquid line of descent defined by groundmass compositions of the three volcanoes (Fig. 2 and 10d). The olivine addition was required to model the mafic mineral compositions observed in the rocks. We modelled polybaric fractional crystallisation from 1400 MPa and 1245°C (liquidus temperature) at the fayalite-magnetite-quartz (FMQ) buffer (Crossingham *et al.,* 2018a) and low water contents of 0.1 to 1.5 wt%, given that > 1.5 wt% H_2O concentrations produced hydrous phases which are not observed in the studied lavas. To assess the validity of Rhyolite-MELTS models, we compared liquid compositions with mafic groundmass compositions, as well as fractionated olivine, clinopyroxene, and plagioclase compositions with the mineral compositions obtained from our mafic samples (following the methodology by Kahl *et al.,* 2015, 2017). Model results show overall agreement with natural data (Fig. 10).

Rhyolite-MELTS results constrain clinopyroxene crystallisation pressure and temperature between 450 to 900 MPa and 850 to 1200°C, respectively (Fig. 10a), in agreement with thermobarometric constraints on pink clinopyroxene-melt pairs (Fig. 9). Plagioclase

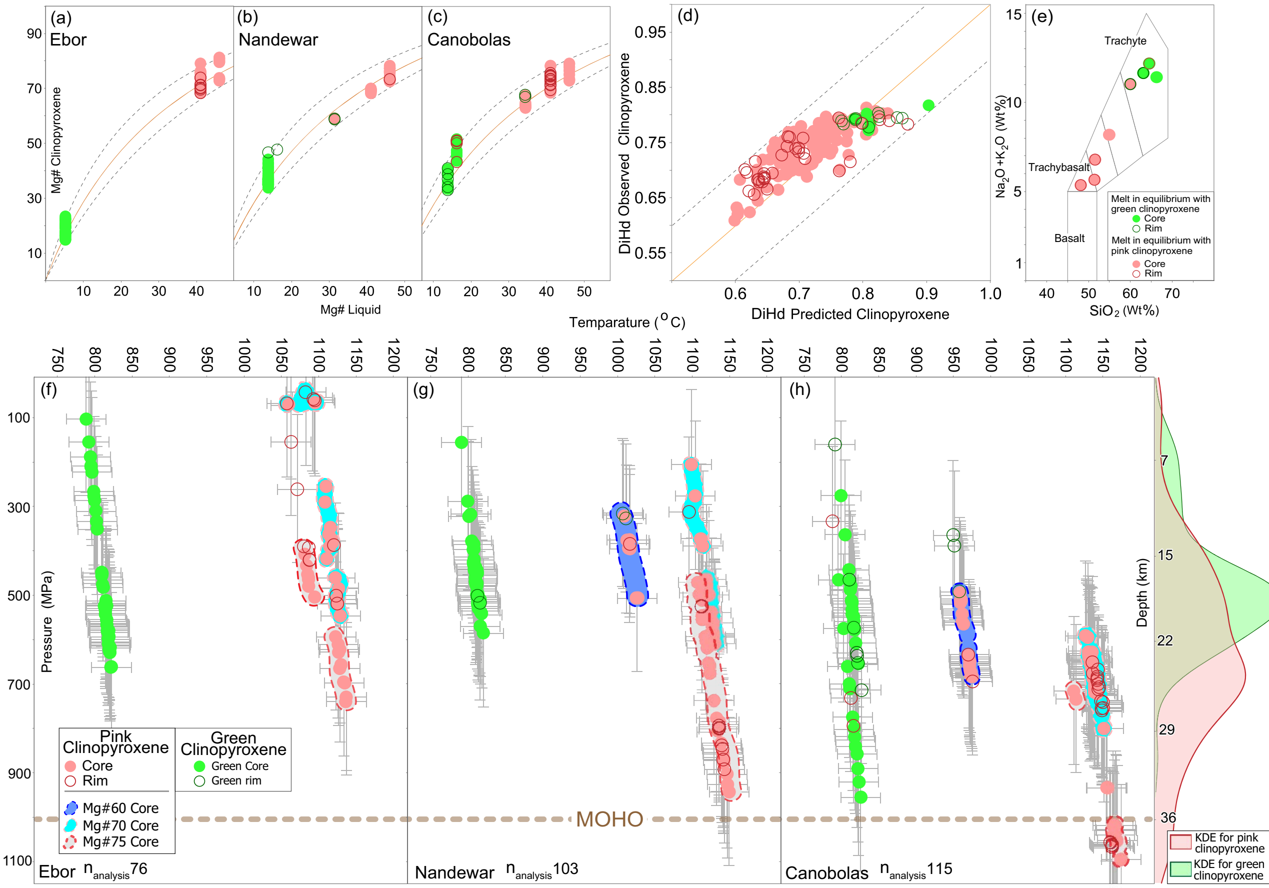

Fig. 9 Clinopyroxene-melt equilibrium tests and thermobarometry estimates for Ebor, Nandewar and Canobolas volcanoes. (a–b–c) Test for Fe-Mg exchange equilibrium for pink and green clinopyroxene cores and rims. Data within the accepted curves (dashed lines) of $Kd_{Fe\text{–}Mg}^{cpx\text{–}melt} = 0.28 \pm 0.08$ (Putirka, 2008) were considered for P–T estimates. (d) Clinopyroxene-melt equilibrium tests comparing measured and predicted DiHd values (Putirka *et al.*, 1996; Mollo *et al.*, 2013). The dashed lines indicate the calibration errors of the models; only data within this range were considered for P–T estimates. (e) Major element TAS classification diagram after Le Bas & Streckeisen (1991) for the equilibrium glass and groundmass compositions from Ebor (sample no Eb5 - glass, Eb12, Eb16), Nandewar (N8, N15, N1) and Canobolas (Ca4, Ca16, Ca13) volcanoes. The pink clinopyroxene cores and rims are in equilibrium with mafic compositions (trachybasalts), whereas the green cores are in equilibrium with felsic varieties (trachytes). (f–g–h) Pressure, temperature and crystallisation depth estimates of clinopyroxene cores and rims of the three volcanoes. We used temperature calibration T1 from Putirka *et al.*, (1996) (pressure-independent, melt-dependent, ±27°C uncertainty, 1σ) and the pressure calibration from Putirka *et al.* (2003) (temperature and melt-dependent, ±170 MPa uncertainty, 1σ). The depth of the MOHO is from Collins *et al.* (2003).

crystallisation pressures and temperatures are slightly lower (350–850 MPa and 750–1200°C; Fig. 10b); however, crystallisation constraints overlap and agree within uncertainties of the simulations (±170 MPa and ± 27°C, respectively; Gualda *et al.*, 2012; Ghiorso & Gualda, 2015). Liquid compositions (Fig. 10c) of the recharge and resident magmas were estimated by comparing Rhyolite-MELTS simulations with data on mafic natural samples. Primitive liquids with Mg#$_{\sim 55}$ produced high Mg# (Mg#$_{75}$) clinopyroxene and high An# (An$_{58\text{–}68}$) plagioclase. More evolved liquids with Mg#$_{25\text{–}35}$ formed Mg#$_{60}$ clinopyroxene and An$_{28\text{–}48}$ plagioclase cores. Increasing water contents promote crystallisation of mafic mineral compositions (Fig. 10), indicating the water-rich nature of recharge magmas relative to resident magmas.

Plagioclase-melt thermobarometry-hygrometry

We applied the models of Putirka (2005, 2008) and France *et al.* (2010) to test P–T conditions of plagioclase crystallisation and link the textural and compositional changes with variations in melt H_2O content and oxidation state ($\log_{\Delta FMQ}$). These models were performed using the same range of melt compositions satisfying clinopyroxene equilibrium tests, as well as melt compositions obtained from Rhyolite–MELTS simulations. Data points falling within the equilibrium envelope for $^{plagioclase\text{–}melt}Kd_{An\text{–}Ab} = 0.28 \pm 0.11$ (Fig. 11a, Putirka, 2008) were used to evaluate melt H_2O contents (Fig. 11b) and in thermobarometric modelling.

All plagioclase compositions return pressures that agree within uncertainties of the calibrations (600–900 MPa, ~18- to 30-km depth; Fig. 11a). The dominant plagioclase cores (An$_{50\text{–}58}$; oscillatory zoned) and the recharge cores (An$_{58\text{–}68}$; slightly rounded) crystallised at higher temperatures (~1180°C) than the low-An cores (An$_{40\text{–}48}$; 1080–1100°C; Fig. 11a). We note that most of the low-An cores (An$_{40\text{–}48}$) with coarse sieved textures did not pass the plagioclase P–T equilibrium test. However, Rhyolite–MELTS simulations suggest colder and shallower conditions as An contents decrease (Fig. 10b).

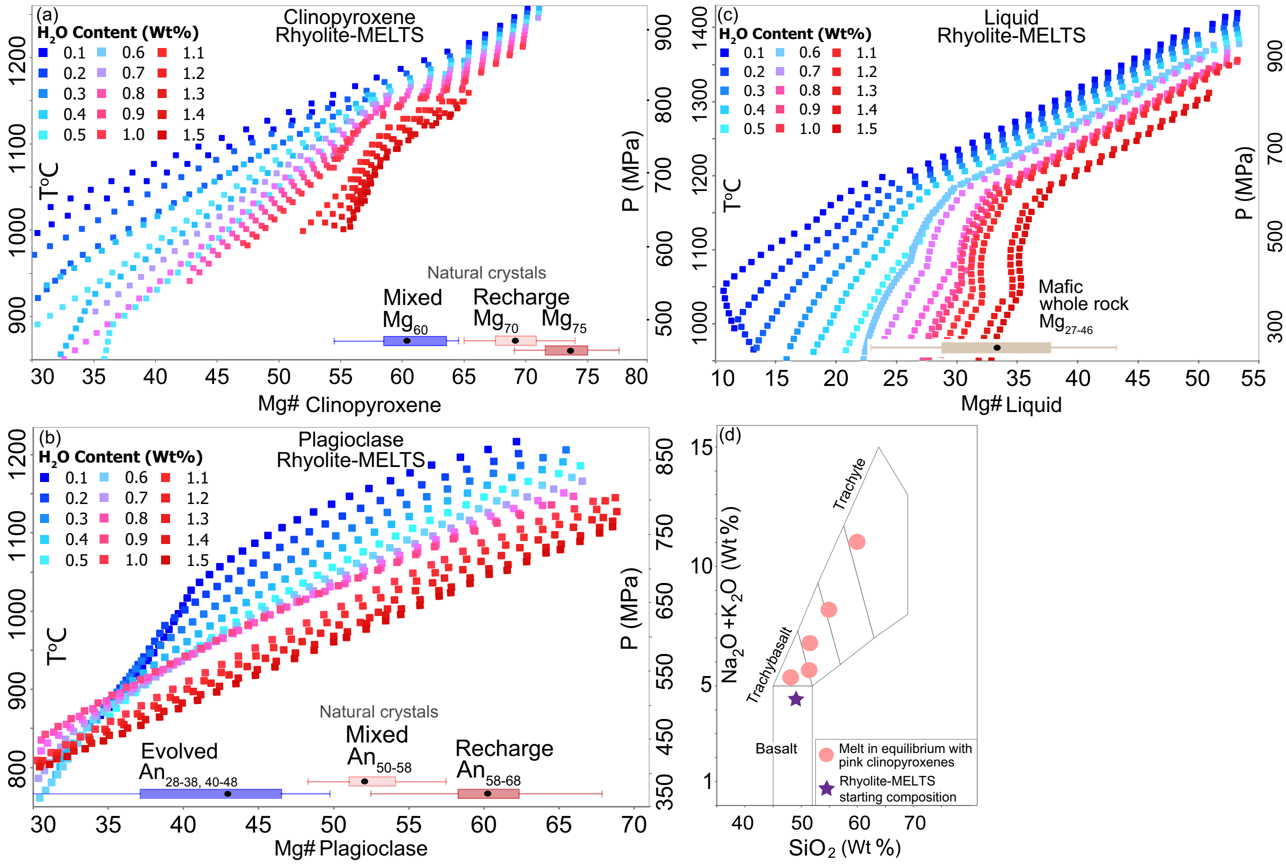

Fig. 10 Summary of Rhyolite-MELTS (Gualda *et al.,* 2012; Ghiorso & Gualda, 2015) simulations. (a–b) Rhyolite-MELTS fractional crystallisation simulations for clinopyroxene and plagioclase. We used starting bulk rock compositions satisfying clinopyroxene equilibrium tests, the quartz-fayalite-magnetite (FMQ) oxygen buffer and variable water contents (0.1 to 1.5 wt% H_2O). Filled squares show modelled clinopyroxene and plagioclase compositions, and the horizontal bar indicates the range of EPMA obtained compositions (black circle indicates median, box area represents 25–75% of the entire dataset). The left and right axes indicate temperature and pressure conditions, respectively. (c) Simulated liquid compositions (Mg#) using variable water contents. The horizontal bar indicates the Mg# range of natural basalts. (d) Starting composition (star symbol) of Rhyolite-MELTS (Gualda *et al.,* 2012; Ghiorso & Gualda, 2015) simulations, together with melts in equilibrium with pink clinopyroxenes (including groundmass separates and glass analyses), plotted on the total alkalis vs silica classification after Le Bas & Streckeisen (1991; TAS, anhydrous).

Modelled liquid-water contents (Fig. 11b) and oxygen fugacities (Fig. 11c) suggest that the main plagioclase population (An_{50-58} cores) crystallised from melts with 1.5–1.9 wt% H_2O and oxygen fugacity conditions around −0.5 to −1 $\log_{\Delta FMQ}$. Magmas that crystallised higher anorthite (An_{58-68}) cores and sieved mantles with higher FeO_t had higher water contents (2.1–2.5 wt%) and were more oxidised (2–3 $\log_{\Delta FMQ}$) than the magmas that produced low An cores (An_{40-48}; 1–1.3 wt% H_2O and − 1 to −2 $\log_{\Delta FMQ}$) (Fig. 11b and c).

Combined with textural and compositional variations, these results indicate that sieve textures record the arrival of mafic magma with higher dissolved H_2O content into the main magma reservoir, as suggested by experimental studies (Phinney, 1992). Such recharge magma might have enhanced the transport of patchy cores formed at deeper conditions than the main plagioclase population (An_{50-58} cores), partially dissolving pre-existing patchy and unzoned cores and overgrowing sieve mantles. The hot recharge magma probably transported high-An cores (An_{58-68}; Fig. 5h), which became slightly rounded with the increase in H_2O pressure upon ascent to the main reservoir.

Reconstruction of the magma plumbing system

The striking similarity of textures and compositions of the crystal cargos from Ebor, Nandewar, and Canobolas volcanoes indicates common pre-eruptive magmatic processes despite contrasting locations, ages, and eruptive volumes. Clinopyroxene–melt thermobarometry, plagioclase–melt hygrometry, and Rhyolite–MELTS return similar conditions of crystallisation across the three volcanoes (Fig. 9), suggesting the development of analogous plumbing systems (Fig. 12).

The prevalence of large plagioclase crystals with mild compositional oscillations among An_{50-58} suggests crystallisation in a main reservoir in the middle crust, under relatively stable magmatic conditions of pressure (600–750 MPa, ~18- to 25-km according to the crustal structure in the region; Collins *et al.,* 2003), temperature (~1100°C), magma composition ($Mg\#_{48-55}$, up to 1.5 wt% H_2O contents) and oxidation state (−0.5 to −1 $\log_{\Delta FMQ}$). Hot (~1200°C) primitive magma (~$Mg\#_{55}$) with relatively high water content (~1.5–2.5 wt%) and oxidation state (~2 $\log_{\Delta FMQ}$) from deeper portions of the plumbing system (800–900 MPa, ~25–30 km) replenished the main reservoir, forming An_{58-68} mantles

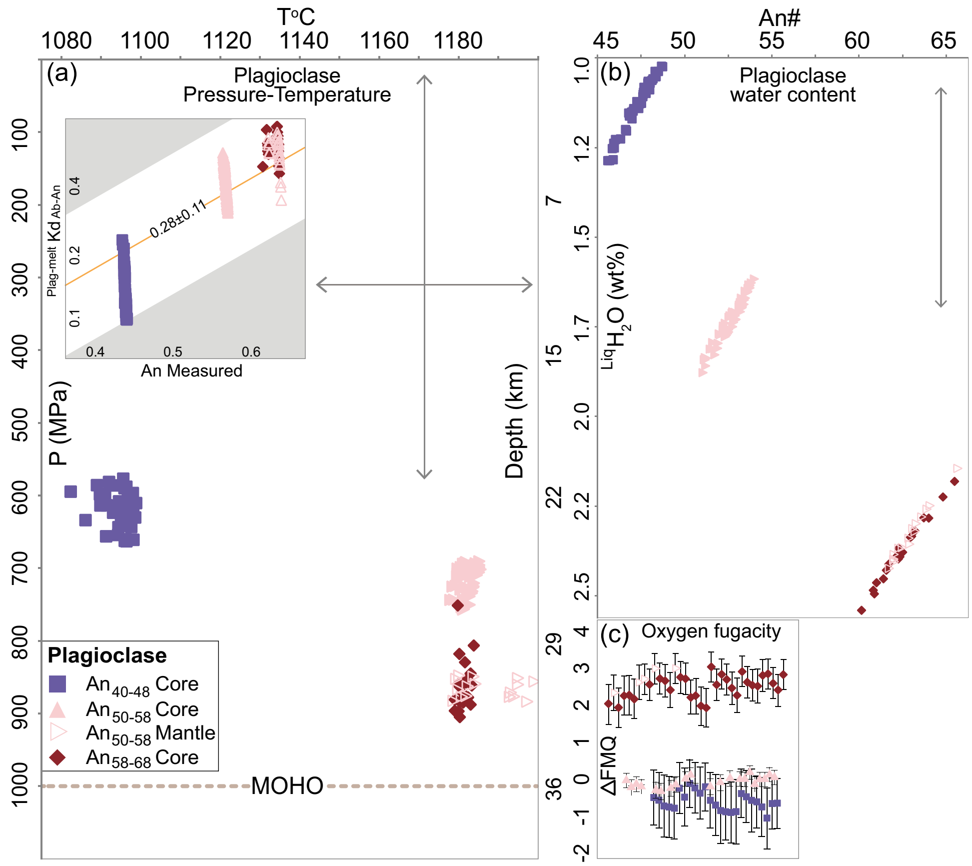

Fig. 11 Plagioclase thermobarometry (Putirka, 2005, 2008) and hygrometry (France *et al.*, 2010). (a) Plagioclase thermobarometry from Putirka (2005, 2008). Input temperatures (1150 to 1225°C for $An_{58–68}$ cores and sieved mantles and 1000–1100 for $An_{40–48}$ cores) were determined from the Rhyolite-MELTS simulations. The inset figure shows plagioclase-melt equilibrium test. (b) Melt water content according to plagioclase-liquid hygrometry (Putirka, 2005), (c) Melt oxygen fugacity (ΔFMQ) calculated from high An plagioclase ($An_{58–68}$ cores, $An_{50–58}$ cores and sieved mantles) and low An plagioclase ($An_{40–48}$ cores) using the model by France *et al.*, (2010).

(sometimes sieved) around $An_{50–58}$ plagioclase cores and ~$Mg\#_{80}$ rims around $Mg\#_{70}$ pink clinopyroxene cores. Magma ascent, enhanced by mafic recharge, possibly led to the development of patchy plagioclase cores and sector-zoned clinopyroxenes. Olivine cores with Fo_{75} might have crystallised from the recharge magma, whereas Fo_{65} olivine cores indicate crystallisation from evolved melts (Supplementary Fig. 4; the complete database is available as Electronic Appendix 1, which may be downloaded from http://www.petrology.oupjournals.org/). Cold pockets of fractionated magmas cogenetic to the plumbing system crystallised green clinopyroxenes and K-feldspars at similar depths (600–800 MPa, ~800°C), and such evolved mushes were incorporated into mafic magma inputs.

The shallower (550–680 MPa, ~15–20 km) portions of the plumbing system possibly crystallised lower An ($An_{40–48}$) plagioclase cores from evolved ($Mg\#_{25–35}$), water-poor (≤1 wt% H_2O), and reduced ($-1 \log_{\Delta FMQ}$) melts. Considering the uncertainties of barometric estimates, the location of such shallow zones would be within the range of depths of the main reservoir ($An_{50–58}$ cores; Fig. 11a). However, we note that large melt pockets entrapped during crystallisation of $An_{40–48}$ coarse sieve cores (Fig. 5c) suggest rapid growth that could have been induced by increased magma undercooling due to degassing (Viccaro *et al.*, 2010; Crabtree & Lange, 2011). Hence, we hypothesise that coarse-sieved, low-An cores could have crystallised above the water saturation level and been recycled by melts ascending from the main reservoir. Finally, plagioclase with the lowest An contents (An_{30}) may represent crystallisation from extremely evolved melts and/or recycling of crustal xenocrysts, as crustal contamination is common in east Australian central volcanoes (Ewart *et al.*, 1977; Ewart, 1989).

Tempos of eruptive pulses and relationships with chemical variations

Variations in mineral textures and chemistry through time reveal recurring changes in magmatic activity throughout the lifespan of the volcanoes (Fig. 13). At Ebor, six lava flows dated between 20.39 ± 0.09 and 20.15 ± 0.08 Ma, and two lava flows dated at 19.97 ± 0.04 and 19.74 ± 0.07 Ma suggest two age clusters of ~0.1 Ma separated by intervals of ~0.1 Ma. Similar tempos of volcanic activity and repose are observed at Nandewar (four lava flows dated between 19.09 ± 0.08 and 19.01 ± 0.04 Ma and four lava flows yielding 18.68 ± 0.05 to 18.51 ± 0.02 Ma) and Canobolas (five lava flows ranging from 11.86 ± 0.04 to 11.55 ± 0.05 Ma; Fig. 13). Geochronological data from the three volcanoes indicate typical eruptive phases and recurrence intervals of ~0.1 Ma (Table 1 and Supplementary Table 3; the complete database is available as Electronic Appendix 1, which may be downloaded from http://www.

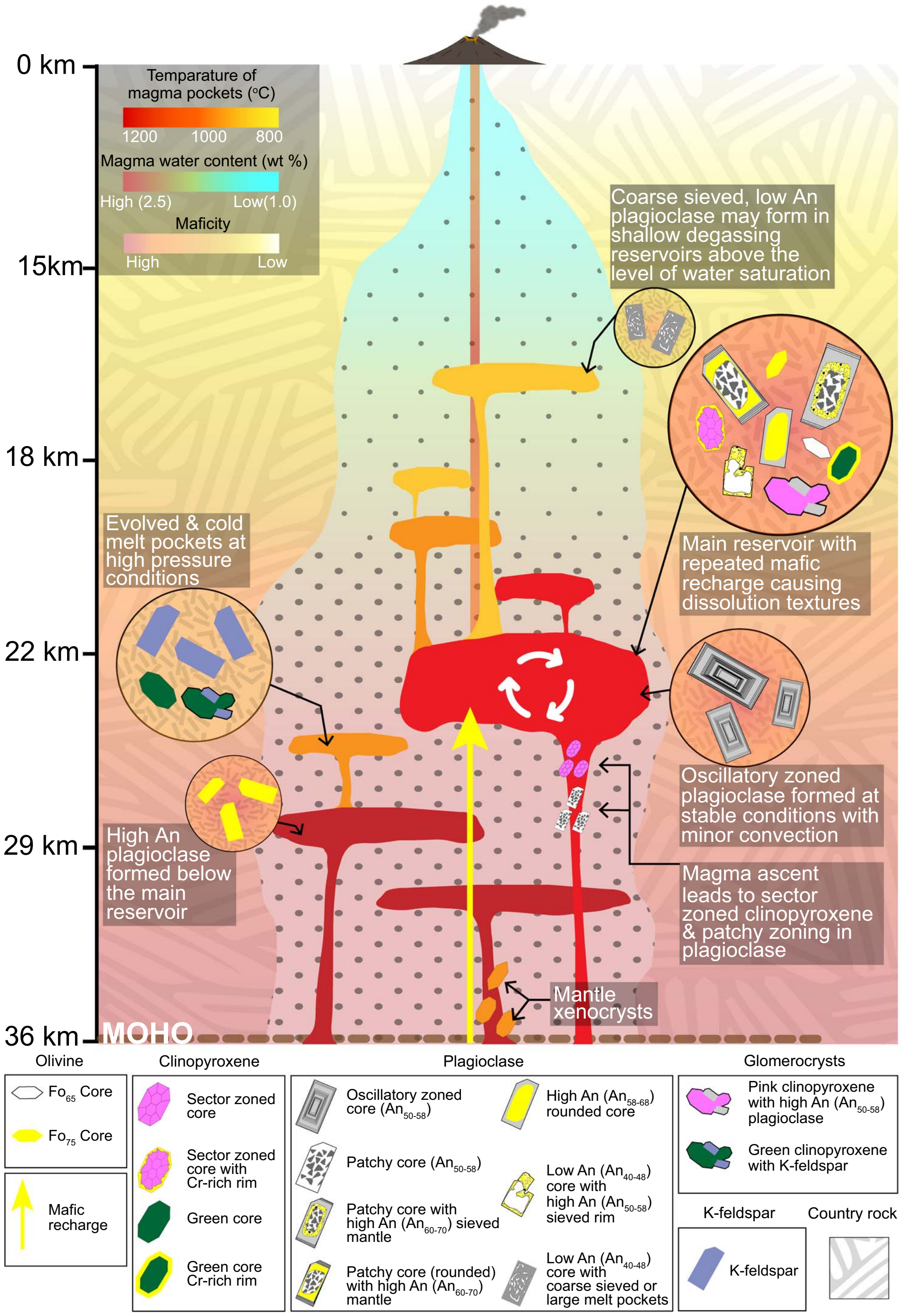

Fig. 12 Simplified model of magma ascent, storage and recharge within different levels of the crust at Ebor, Nandewar and Canobolas Cenozoic volcanoes in east Australia. At mid-crustal levels and undegassed conditions, the main plagioclase population ($An_{50–58}$) with oscillatory zoning crystallised within the main storage system at ~18–25 km depth, possibly consisting of undisturbed reservoirs with soft convective movements. Sector-zoned clinopyroxene cores and patchy zoned plagioclase cores possibly crystallised in relation to slow magma ascent into such main reservoir/s. Hot, primitive recharge magmas produced dissolution features in pre-existing plagioclase and clinopyroxene cores and brought in mafic cores. Evolved, cool magma reservoirs led to crystallisation of green clinopyroxene and K-feldspar phenocryst cores as glomerocrysts at ~18–30 km. Crystallisation continued in shallow portions (~15–20 km) of the plumbing system, where degassing increased the degree of undercooling and potentially induced fast crystallisation of low-An ($An_{40–48}$) plagioclase with entrapment of large melt pockets, generating coarse sieved textures. MOHO depth from Collins *et al.* (2003).

petrology.oupjournals.org/). We acknowledge potential sampling bias and consider our durations of eruptive pulses as minima and repose periods as maxima; however, the comprehensive stratigraphic sampling and consistency of age results across three volcanoes support the rhythmic ~0.1 Ma volcanic tempos. Interestingly, younger (late Neogene to Quaternary), non-age progressive volcanic centres from northern Queensland show recurring intervals that are one order of magnitude lower (10 to 22 ka; Cohen *et al.*, 2017).

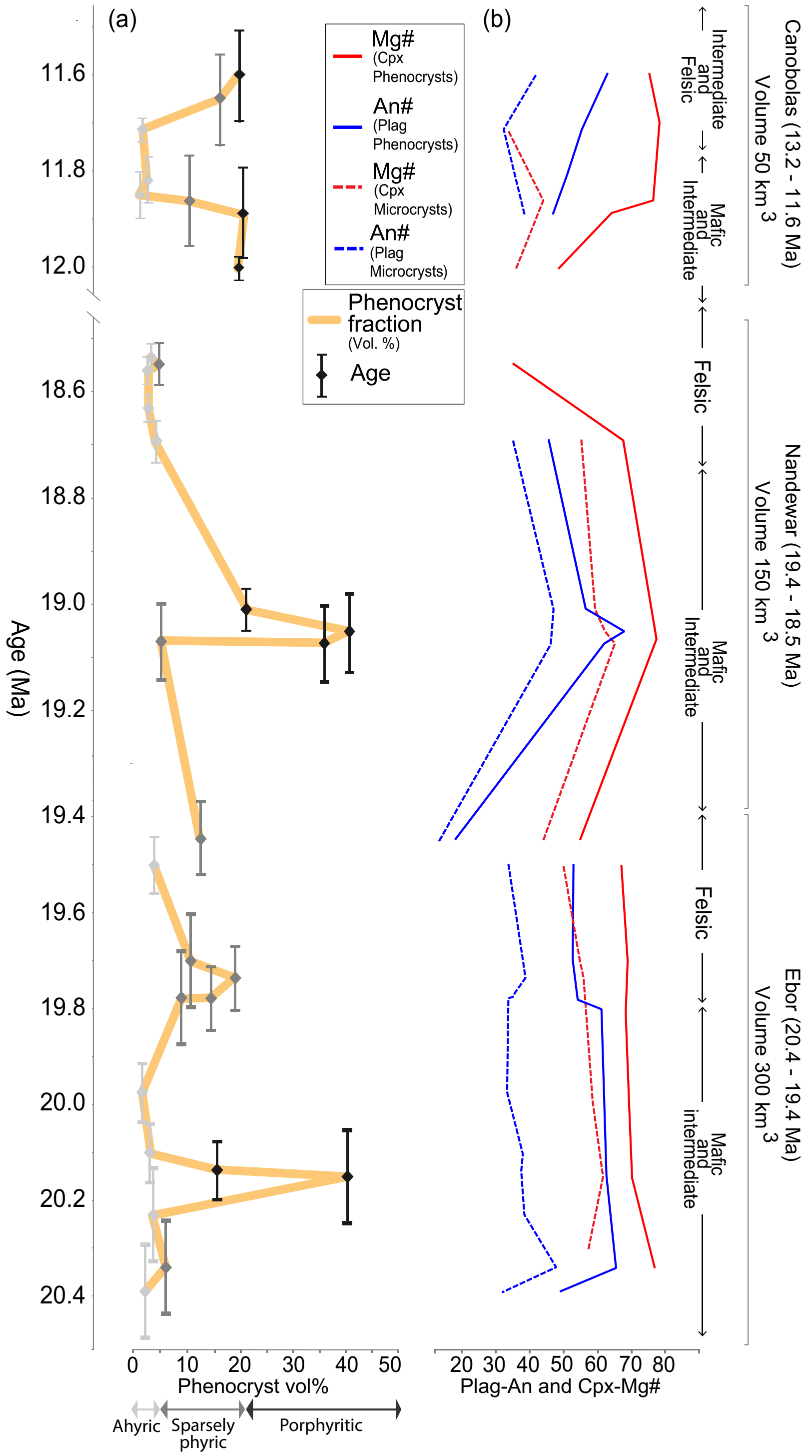

Fig. 13 Variations in porphyricity (a) and mineral compositions (b: An in plagioclase and Mg# in pink clinopyroxene) with time in Ebor, Nandewar and Canobolas volcanoes. Crystal-rich samples correlate with high-An and high-Mg# contents, highlighting the key role of mafic recharge in mush disaggregation and eruption triggering.

Consistently, the composition of erupted lavas changes from mafic at the base of the stratigraphy to intermediate and felsic towards the end of eruptive activity (Figs. 2 and 13). The volcanostratigraphic sequences investigated show a marked increase in porphyricity (volume fraction of phenocrysts) at the early-middle stages in Ebor and Nandewar and towards the late stages of the studied Canobolas activity (Fig. 13a). Across all three volcanoes, lavas with the highest porphyricity are associated with high-An ($An_{50–58}$ and $An_{58–68}$) plagioclase and high-Mg# ($Mg\#_{60–75}$) pink clinopyroxene, including both phenocrysts and groundmass microcrysts (Fig. 13b). These high-An and high-Mg# compositions are associated with dissolution textures in phenocrysts (Cr-rich clinopyroxene rims and sieved plagioclase mantles) that agree with mafic magma recharge events, as discussed above (see sections 6.1 and 6.2).

The correlation between rock porphyricity and magma recharge highlights the role of mafic replenishment in mush remobilisation and eruption triggering. Petrological cannibalism is commonly reported in active arc systems, where repeated mafic injections disrupt shallow crystal mushes and modulate eruptive activity, producing plagioclase and clinopyroxene cargoes with resorption textures (Reubi & Blundy, 2008; Cashman & Blundy, 2013; Di Stefano *et al.,* 2020). For example, at Stromboli volcano (Italy), periodic infiltration of crystal-poor magmas causes continuous disruption and cannibalisation of old clinopyroxenes mushes at different depths, generating continuous cycles of mafic injection, magma mixing, and homogenisation that vary in efficiency through time (Petrone *et al.,* 2018; Di Stefano *et al.,* 2020). Our data from eastern Australia highlight the relevance of recurrent magma recharges in mush dynamics in an intraplate continental setting. Mafic replenishment leads to mush disaggregation and eruption of lavas with increased porphyricity and complex textural variations. The reduction in porphyricity towards the end of the volcanic lifespans at Ebor and Nandewar could be linked to a reduction in magma supply, leading to magma differentiation in the plumbing system and eruption of more evolved lavas. We note that the change in porphyricity was not identical in Canobolas, perhaps due to mafic recharge events close to the end of its lifespan. Regardless, the observed variations of magma composition and porphyricity through volcanism (Fig. 13) could reflect the role of magmatic fluxes in driving the birth, climax, and death of volcanic plumbing systems.

Similar petrological variations are observed in other central volcanoes located towards the end of the age progressive track in eastern Australia. The Warrumbungle and Comboyne volcano pair, situated at latitudes intermediate between the volcanoes studied here (Fig. 1; 17.0 ± 0.1 to 15.5 ± 0.2 Ma), was also fed by complex plumbing systems with magma stagnation at different levels in the crust and cyclic mafic magma recharge events producing texturally and compositionally complex phenocryst assemblages (Crossingham *et al.,* 2018a). The similar complexity in plumbing mechanisms in the south contrasts with relatively simple magma ascent described at the Buckland volcano to the north of the track (Fig. 1; Crossingham *et al.,* 2018b), suggesting that waning hotspot activity may be associated with complex magma transport and storage in intraplate continental settings. Future work will investigate if such relationships hold across the age-progressive volcanic belt.

CONCLUSIONS

We have investigated the lifespan of volcanic activity and pre-eruptive magmatic histories at Ebor, Nandewar, and Canobolas volcanoes formed during waning Cenozoic hotspot activity in eastern Australia. The integration of high-resolution $^{40}Ar/^{39}Ar$ geochronology, major and trace element mineral chemistry, clinopyroxene–melt thermobarometry, plagioclase–melt thermometry and hygrometry, and Rhyolite–MELTS simulations make it possible to link magmatic processes to tempos of age-progressive volcanic activity.

$^{40}Ar/^{39}Ar$ geochronology constrains the duration of volcanic activity at ~0.5 to 1.0 Ma for the samples collected in each of the volcanic centres (Ebor, 20.39 ± 0.09 to 19.39 ± 0.07 Ma; Nandewar, 19.43 ± 0.03 to 18.45 ± 0.03 Ma; Canobolas, 12.01 ± 0.02 to 11.55 ± 0.05 Ma), similar to other age-progressive systems located towards the end of the eastern Australia hotspot track. Eruptive products evolved through time, and cyclic mafic magma replenishment was a critical driver of mush disaggregation and eruption of porphyritic lavas with complex crystal cargoes.

Feldspar and clinopyroxene phenocryst populations reflect magma storage in the crust and magma transport fuelled by frequent mafic injections and crystal recycling, sometimes sampling evolved magma pockets. We interpret a main reservoir at 18- to 25-km depth, generating oscillatory zoned plagioclase and pink clinopyroxene phenocrysts. Periodically, replenishments of mafic hot magma generated a wide range of textural and compositional variations in crystallising minerals, such as high-An mantles in plagioclase and high–Mg–Cr-rich rims in clinopyroxene. Magma ascent due to recharge may have led to the formation of patchy zones in plagioclase cores and sector zoning in pink clinopyroxene cores. Uptake and transport of evolved crystals from low temperature crystallising bodies were also initiated by the mafic rejuvenation events. At shallow levels, magma water loss may have led to increased undercooling and rapid crystallisation of plagioclase phenocrysts that trapped large melt inclusions, producing coarse sieved textures. Plagioclase phenocrysts with the lowest An contents may represent crustal xenocrysts or crystallisation from extremely evolved melts, similar to K-feldspar phenocrysts.

Our comprehensive approach, including $^{40}Ar/^{39}Ar$ geochronology, high-resolution petrology and geochemistry, together with thermodynamic modelling, indicates that continental intraplate volcanoes linked to waning hotspot activity have relatively short eruptive lifespans (~1 Ma) with bursts of activity driven by mafic magma recharge that are one order of magnitude shorter (~0.1 Ma). These characteristics apply to volcanoes active across a total of ~8 million years, developed in crust and lithosphere settings of similar thicknesses. Results from this study open an exciting opportunity to explore regional variations in volcanic tempos and plumbing system architecture across the entire lifetime of hotspot activity in east Australia and other plume-related tracks globally.

SUPPLEMENTARY DATA

Supplementary data are available at *Journal of Petrology* online.

FUNDING

This work was supported by The University of Queensland Argon Laboratory (UQ AGES, P.V.) and a Foundation Research Excellence Award from The University of Queensland (UQ-FREA RM2019001828, TU). A.T.T. acknowledges the support from the Australian Government Research Training Program (UQRTP; PhD scholarship).

ACKNOWLEDGEMENTS

We thank the NSW National Parks and Wildlife Service (licence number SL101471) for sampling permits and the staff at the National Parks and Wildlife Service for their assistance. We thank Tracey Crossingham, Isabelle Jones, Llyam White, and Oliver Turner for the sampling. We thank Tracey Crossingham for her assistance with microprobe analysis and insightful discussions while preparing this manuscript, John Caulfield for his assistance with laser ablation ICP-MS analysis, David Thiede for his assistance with $^{40}Ar/^{39}Ar$ analysis, Allan Gomes for his assistance interpreting $^{40}Ar/^{39}Ar$ data, Ai Nguyen for his assistance with groundmass analysis and Gang Xia for his assistance with thin section preparation. We acknowledge the facilities and staff of the Australian Microscopy & Microanalysis Research Facility at the Centre for

Microscopy and Microanalysis (CMM), The University of Queensland. We highly appreciate constructive reviews from S. Mollo, M. Mangler and three anonymous reviewers, which helped us improve the original version of the paper, as well as editorial handling by A. Kent and G. Zellmer.

REFERENCES

Allègre, C. J., Provost, A. & Jaupart, C. (1981). Oscillatory zoning: a pathological case of crystal growth. *Nature* **294**, 223–228.

Ashley, P. M., Duncan, R. A. & Feebrey, C. A. (1995). Ebor volcano and crescent complex, northeastern New South Wales: age and geological development. *Australian Journal of Earth Sciences* **42**, 471–480.

Baker, D. R. (2008). The fidelity of melt inclusions as records of melt composition. *Contributions to Mineralogy and Petrology* **156**, 377–395.

Ball, P. W., Czarnota, K., White, N. J., Klöcking, M. & Davies, D. R. (2021). Thermal structure of eastern Australia's upper mantle and its relationship to Cenozoic volcanic activity and dynamic topography. *Geochemistry, Geophysics, Geosystems* **22**.

Bennett, E. N., Lissenberg, C. J. & Cashman, K. V. (2019). The significance of plagioclase textures in mid-ocean ridge basalt (Gakkel ridge, Arctic Ocean). *Contributions to Mineralogy and Petrology* **49**.

Bergantz, G. W., Schleicher, J. M. & Burgisser, A. (2015). Open-system dynamics and mixing in magma mushes. *Nature Geoscience* **8**, 793–796.

Blundy, J. & Cashman, K. (2001). Ascent-driven crystallisation of dacite magmas at mount st Helens, 1980-1986. *Contributions to Mineralogy and Petrology* **140**, 631–650.

Cao, M., Evans, N. J., Reddy, S. M., Fougerouse, D., Hollings, P., Saxey, D. W., McInnes, B. I., Cooke, D. R., McDonald, B. J. & Qin, K. (2019). Micro-and nano-scale textural and compositional zonation in plagioclase at the Black Mountain porphyry cu deposit: implications for magmatic processes. *Mineralogical Society of America*(3) **104**, 391–402.

Cashman, K. & Blundy, J. (2013). Petrological cannibalism: the chemical and textural consequences of incremental magma body growth. *Contributions to Mineralogy and Petrology* **166**, 703–729.

Cashman, K. V., Sparks, R. S. J. & Blundy, J. D. (2017). Vertically extensive and unstable magmatic systems: a unified view of igneous processes. *Science* **355**, 3055.

Cohen, B. E. (2002) *Geochronology and Geochemistry of southeast Queensland Tertiary Volcanism*. B.Sc. (Hons.), University of Queensland, Brisbane (unpubl.).

Cohen, B. E. (2007) *High-resolution 40Ar/39Ar geochronology of intraplate volcanism in eastern Australia*. University of Queensland, Brisbane, Australia: School of Earth Sciences.

Cohen, B. E., Knesel, K. M., Vasconcelos, P. M. & Schellart, W. P. (2013). Tracking the Australian plate motion through the Cenozoic: constraints from 40 ar/ 39 ar geochronology. *Tectonics* **32**, 1371–1383.

Cohen, B. E., Knesel, K. M., Vasconcelos, P. M., Thiede, D. S. & Hergt, J. M. (2008). ^{40}Ar/ ^{39}Ar constraints on the timing and origin of Miocene leucitite volcanism in southeastern Australia. *Australian Journal of Earth Sciences* **55**, 407–418.

Cohen, B. E., Mark, D. F., Fallon, S. J. & Stephenson, P. J. (2017). Holocene-Neogene volcanism in northeastern Australia: chronology and eruption history. *Quaternary Geochronology* **39**, 79–91.

Collins, C. D. N., Drummond, B. J. & Nicoll, M. G. (2003) Crustal thickness patterns in the Australian continent. In: (Hills R. R. & Muller R. D. (eds)) *Evolution and Dynamics of the Australian Plate. Geological SocietyofAustralia, Special Publication 22; GeologicalSocietyofAmerica, Special Papers*, Vol. **372**, pp.121–128.

Costa, F. (2021). Clocks in magmatic rocks. *Annual Review of Earth and Planetary Sciences* **49**, 231–252.

Couch, S., Sparks, R. S. J. & Carroll, M. R. (2001). Mineral disequilibrium in lavas explained by convective self-mixing in open magma chambers. *Nature* **411**, 1037–1039.

Crabtree, S. M. & Lange, R. A. (2011). Complex Phenocryst textures and zoning patterns in Andesites and Dacites: evidence of degassing-induced rapid crystallization? *Journal of Petrology* **52**, 3–38.

Crossingham, T., Ubide, T., Vasconcelos, P. & Mallmann, G. (2018a). Parallel plumbing systems feeding a pair of coeval volcanoes in eastern Australia. *Journal of Petrology* **59**, 1035–1066.

Crossingham, T. J., Ubide, T., Vasconcelos, P. M., Knesel, K. M. & Mallmann, G. (2018b). Temporal constraints on magma generation and differentiation in a continental volcano: Buckland, eastern Australia. *Lithos* **302**, 341–358.

Davies, D. R., Rawlinson, N., Iaffaldano, G. & Campbell, I. H. (2015). Lithospheric controls on magma composition along Earth's longest continental hotspot track. *Nature* **525**, 511–514.

Deer, W., Howie, R. & Zussman, J. (1978). Rock-forming minerals. *2A. Single-Chain Silicates* **281**, 668.

Deino, A. & Potts, R. (1992). Age-probability spectra for examination of single-crystal dating results: Examples from Olorgesailie, southern Kenya Rift. *Quaternary International* **13-14**, 47–53.

Di Stefano, F., Mollo, S., Ubide, T., Petrone, C. M., Caulfield, J., Scarlato, P., Nazzari, M., Andronico, D. & Del Bello, E. (2020). Mush cannibalism and disruption recorded by clinopyroxene phenocrysts at Stromboli volcano: new insights from recent 2003-2017 activity. *Lithos* **360-361**, 105440.

Downes, M. J. (1974). Sector and oscillatory zoning in calcic augites from M. Etna, Sicily. *Contributions to Mineralogy and Petrology* **47**, 187–196.

Duda, A. & Schmincke, H. U. (1985). Polybaric differentiation of alkali basaltic magmas: evidence from green-core clinopyroxenes (Eifel, FRG). *Contributions to Mineralogy and Petrology* **91**, 340–353.

Edmonds, M., Cashman, K. V., Holness, M. & Jackson, M. (2019). Architecture and dynamics of magma reservoirs. *The Royal Society Publishing* **377**, 20180298.

Ewart, A. (1989) Mineralogy and mineral chemistry. In: (Johnson R. W. (ed)) *Intraplate Volcanism in Eastern Australia and New Zealand*. Cambridge: Cambridge University Press, pp.197–215.

Ewart, A., Chappell, B. W. & Menzies, M. A. (1988). An overview of the geochemical and isotopic characteristics of the eastern Australian Cainozoic volcanic provinces. *Journal of Petrology* **Special Volume**, 225–273.

Ewart, A., Oversby, V. M. & Mateen, A. (1977). Petrology and isotope geochemistry of tertiary lavas from the northern flank of the tweed volcano, southeastern Queensland. *Journal of Petrology* **18**, 73–113.

Ewart, A. & Stevens, N. (1987) *The Tweed and Focal Peak Shield Volcanoes, Southeast Queensland and Northeast New South Wales*. Department of Geology, University of Queensland.

Fishwick, S., Heintz, M., Kennett, B., Reading, A. & Yoshizawa, K. (2008). Steps in lithospheric thickness within eastern Australia, evidence from surface wave tomography. *Tectonics* **27**.

Fleck, R. J., Sutter, J. F. & Elliot, D. H. (1977). Interpretation of discordant 40Ar/39Ar age-spectra of mesozoic tholeiites from Antarctica. *Geochimica et Cosmochimica Acta* **41**, 15–32.

France, L., Ildefonse, B., Koepke, J. & Bech, F. (2010). A new method to estimate the oxidation state of basaltic series from microprobe analyses. *Journal of Volcanology and Geothermal Research* **189**, 340–346.

Ghiorso, M. S. & Gualda, G. A. R. (2015). An H_2O-CO_2 mixed fluid saturation model compatible with rhyolite-MELTS. *Contributions to Mineralogy and Petrology* **169**, 53.

Giacomoni, P. P., Ferlito, C., Coltorti, M., Bonadiman, C. & Lanzafame, G. (2014). Plagioclase as archive of magma ascent dynamics on 'open conduit' volcanoes: the 2001–2006 eruptive period at Mt. Etna. *Earth-Science Reviews* **138**, 371–393.

Gualda, G. A. R., Ghiorso, M. S., Lemons, R. V. & Carley, T. L. (2012). Rhyolite- MELTS: a modified calibration of MELTS optimised for silica-rich, fluid-bearing magmatic systems. *Journal of Petrology* **53**, 875–890.

Johnson, R. W. (1989) Volcano distribution and classification. In: (Johnson R. W. (ed)) *Intraplate Volcanism in Eastern Australia and New Zealand*. Cambridge: Cambridge University Press, pp.189–384.

Jones, I., Ubide, T., Crossingham, T., Wilding, B. & Verdel, C. (2020). Evidence of a common source component for east Australian Cenozoic mafic magmatism. *Lithos* **354-355**, 105–254.

Jones, I. & Verdel, C. (2015). Basalt distribution and volume estimates of Cenozoic volcanism in the Bowen Basin region of eastern Australia:

implications for a waning mantle plume. *Australian Journal of Earth Sciences* **62**, 255–263.

Jones, I., Verdel, C., Crossingham, T. & Vasconcelos, P. (2017). Animated reconstructions of the late cretaceous to Cenozoic northward migration of Australia, and implications for the generation of east Australian mafic magmatism. *Geosphere (Boulder, Colo.)* **13**, 460–481.

Jones, I. M. (2018) *Evolution and migration of Cenozoic Australia: precision $^{40}Ar/^{39}Ar$ geochronology, geochemistry and paleomagnetic data from east Australian Cenozoic magmas*. The University of Queensland, School of Earth and Environmental Sciences.

Kahl, M., Chakraborty, S., Pompilio, M. & Costa, F. (2015). Constraints on the nature and evolution of the magma plumbing system of Mt. Etna volcano (1991-2008) from a combined thermodynamic and kinetic modelling of the compositional record of minerals. *Journal of Petrology* **56**, 2025–2068.

Kahl, M., Chakraborty, S., Costa, F. & Pompilio, M. (2011). Dynamic plumbing system beneath volcanoes revealed by kinetic modeling, and the connection to monitoring data: an example from Mt. Etna. *Earth and Planetary Science Letters* **308**, 11–22.

Kahl, M., Viccaro, M., Ubide, T., Morgan, D. J. & Dingwell, D. B. (2017). A branched magma feeder system during the 1669 eruption of Mt Etna: evidence from a time-integrated study of zoned olivine phenocryst populations. *Journal of Petrology* **58**, 443–472.

Kirkpatrick, R. J., Klein, L., Uhlmann, D. R. & Hays, J. F. (1979). Rates and processes of crystal growth in the system anorthite-albite. *Journal of Geophysical Research: Solid Earth* **84**, 3671–3676.

Klügel, A., Day, S., Schmid, M. & FAria, B. (2020). Magma plumbing during the 2014-2015 eruption of Fogo (Cape Verde Islands). *Frontiers in Earth Science* **8**.

Knesel, K. M., Cohen, B. E., Vasconcelos, P. M. & Thiede, D. S. (2008). Rapid change in drift of the Australian plate records collision with Ontong Java plateau. *Nature* **454**, 754–757.

Kouchi, A., Sugawara, Y., Kashima, K. & Sunagawa, I. (1983). Laboratory growth of sector zoned clinopyroxenes in the system CaMgSi2O6-CaTiAl2O6. *Contributions to Mineralogy and Petrology* **83**, 177–184.

Kuiper, K. F., Deino, A., Hilgen, F. J., Krijgsman, W., Renne, P. R. & Wijbrans, J. R. (2008). Synchronizing rock clocks of earth history. *Science* **320**, 500–504.

Larrea, P., Albert, H., Ubide, T., Costa, F., Colás, V., Widom, E. & Siebe, C. (2021). From explosive vent opening to effusive outpouring: mineral constraints on magma dynamics and timescales at paricutin monogenetic volcano. *Journal of Petrology* **62**, 112.

Le Bas, M. & Streckeisen, A. L. (1991). The IUGS systematics of igneous rocks. *Journal of the Geological Society* **148**, 825–833.

Lee, J.-Y., Marti, K., Severinghaus, J. P., Kawamura, K., Yoo, H.-S., Lee, J. B. & Kim, J. S. (2006). A redetermination of the isotopic abundances of atmospheric ar. *Geochimica et Cosmochimica Acta* **70**, 4507–4512.

Leung, I. S. (1974). Sector-zoned titanaugites: morphology, crystal chemistry, and growth. *American Mineralogist: Journal of Earth and Planetary Materials* **59**, 127–138.

Lofgren, G. (1980). Experimental studies on the dynamic crystallisation of silicate melts. *Physics of Magmatic Processes* **487**, 551.

Magee, R., Ubide, T. & Caulfield, J. (2021). Days to weeks of syn-eruptive magma interaction: high-resolution geochemistry of the 2002-03 branched eruption at Mount Etna. *Earth and Planetary Science Letters* **565**, 116904.

Masotta, M., Pontesilli, A., Mollo, S., Armienti, P., Ubide, T., Nazzari, M. & Scarlato, P. (2020). The role of undercooling during clinopyroxene growth in trachybasaltic magmas: insights on magma decompression and cooling at Mt. Etna volcano. *Geochimica et Cosmochimica Acta* **268**, 258–276.

Middlemost, E. A. K. (1981). The Canobolas complex, N.S.W., an alkaline shield volcano. *Journal of the Geological Society of Australia* **28**, 33–49.

Mollo, S., Blundy, J., Iezzi, G., Scarlato, P. & Langone, A. (2013). The partitioning of trace elements between clinopyroxene and trachybasaltic melt during rapid cooling and crystal growth. *Contributions to Mineralogy and Petrology* **166**, 1633–1654.

Mollo, S. & Masotta, M. (2014). Optimising pre-eruptive temperature estimates in thermally and chemically zoned magma chambers. *Chemical Geology* **368**, 97–103.

Mollo, S., Ubide, T., Di Stefano, F., Nazzari, M. & Scarlato, P. (2020). Polybaric/polythermal magma transport and trace element partitioning recorded in single crystals: a case study of a zoned clinopyroxene from Mt. Etna. *Lithos* **356-357**, 105382.

Nakamura, M. & Shimakita, S. (1998). Dissolution origin and syn-entrapment compositional change of melt inclusion in plagioclase. *Earth and Planetary Science Letters* **161**, 119–133.

Nakamura, Y. (1973). Origin of sector-zoning of igneous Clinopyroxenes. *American Mineralogist* **58**, 986–990.

Neave, D. A., Bali, E., Guðfinnsson, G. H., Halldórsson, S. A., Kahl, M., Schmidt, A.-S. & Holtz, F. (2019). Clinopyroxene-liquid equilibria and Geothermobarometry in natural and experimental Tholeiites: the 2014-2015 Holuhraun eruption, Iceland. *Journal of Petrology* **60**, 1653–1680.

Nelson, S. T. & Montana, A. (1992). Sieve-textured plagioclase in volcanic rocks produced by rapid decompression. *American Mineralogist* **77**, 1242–1249.

Newhall, C. G. (1979). Temporal variation in the lavas of Mayon volcano, Philippines. *Journal of Volcanology and Geothermal Research* **6**, 61–83.

Paton, C., Hellstrom, J., Paul, B., Woodhead, J. & Hergt, J. (2011). Iolite: freeware for the visualisation and processing of mass spectrometric data. *Journal of Analytical Atomic Spectrometry* **26**, 2508.

Pearce, T., Russell, J. & Wolfson, I. (1987). Laser-interference and Nomarski interference imaging of zoning profiles in plagioclase phenocrysts from the may 18, 1980, eruption of Mount St. Helens, Washington. *American Mineralogist* **72**, 1131–1143.

Petrus, J. A., Chew, D. M., Leybourne, M. I. & Kamber, B. S. (2017). A new approach to laser-ablation inductively-coupled-plasma mass-spectrometry (LA-ICP-MS) using the flexible map interrogation tool 'Monocle'. *Chemical Geology* **463**, 76–93.

Petrone, C. M., Braschi, E., Francalanci, L., Casalini, M. & Tommasini, S. (2018). Rapid mixing and short storage timescale in the magma dynamics of a steady-state volcano. *Earth and Planetary Science Letters* **492**, 206–221.

Phinney, W. C. (1992). Partition coefficients for iron between plagioclase and basalt as a function of oxygen fugacity: implications for Archean and lunar anorthosites. *Geochimica et Cosmochimica Acta* **56**, 1885–1895.

Pizarro, C., Parada, M. A., Contreras, C. & Morgado, E. (2019). Cryptic magma recharge associated with the most voluminous 20th century eruptions (1921, 1948 and 1971) at Villarrica volcano. *Journal of Volcanology and Geothermal Research* **384**, 48–63.

Putirka, K., Johnson, M., Kinzler, R., Longhi, J. & Walker, D. (1996). Thermobarometry of mafic igneous rocks based on clinopyroxene-liquid equilibria, 0-30 kbar. *Contributions to Mineralogy and Petrology* **123**, 92–108.

Putirka, K. D., Mikaelian, H., Ryerson, F. & Shaw, H. (2003). New clinopyroxene- liquid thermobarometers for mafic, evolved, and volatile-bearing lava compositions, with applications to lavas from Tibet and the Snake River plain, Idaho. *American Mineralogist* **88**, 1542–1554.

Putirka, K. D. (2005). Igneous thermometers and barometers based on plagioclase+ liquid equilibria: tests of some existing models and new calibrations. *American Mineralogist* **90**, 336–346.

Putirka, K. (2008). Thermometers and barometers for volcanic systems. In: Putirka, K.D. & Tepley, F. J., III, (eds) *Minerals, InclusionsandVolcanic Processes. Mineralogical Society of America and Geochemical Society, Reviews in Mineralogy and Geochemistry* **69**, 61–120

Reubi, O. & Blundy, J. (2008). Assimilation of plutonic roots, formation of high-K 'exotic'melt inclusions and genesis of andesitic magmas at Volcán de Colima, Mexico. *Journal of Petrology* **49**, 2221–2243.

Sparks, R. S. J. & Pinkerton, H. (1978). Effect of degassing on rheology of basaltic lava. *Nature* **276**, 385–386.

Spell, T. L. & McDougall, I. (2003). Characterization and calibration of 40Ar/39Ar dating standards. *ChemicalGeology* **198**, 189–211.

Stipp, J. & McDougall, I. (1968). Potassium-argon ages from the Nandewar volcano, near Narrabri. *New South Wales. Australian Journal of Science* **31**, 84–85.

Stock, M. J., Geist, D., Neave, D. A., Gleeson, M. L. M., Bernard, B., Howard, K. A., Buisman, I. & Maclennan, J. (2020). Cryptic evolved melts beneath monotonous basaltic shield volcanoes in the Galápagos archipelago. *Nature Communications* **11**, 3767.

Stolz, A. J. (1986). Mineralogy of the Nandewar volcano, northeastern New South Wales, Australia. *Mineralogical Magazine* **50**, 241–255.

Stolz, A. J. (1985). The role of fractional crystallisation in the evolution of the Nandewar volcano, North-Eastern New South Wales, Australia. *Journal of Petrology* **26**, 1002–1026.

Streck, M. J. (2008). Mineral textures and zoning as evidence for open system processes. *Reviews in Mineralogy and Geochemistry* **69**, 595–622.

Sun, S., McDonough, W. & Ewart, A. (1989) *Four component model for east Australian basalts. Intraplate volcanism in eastern Australia and New Zealand*. Cambridge: Cambridge University Press, pp. 333–347.

Sutherland, F. L., Graham, I. T., Meffre, S., Zwingmann, H. & Pogson, R. E. (2012). Passive-margin prolonged volcanism, east Australian plate: outbursts, progressions, plate controls and suggested causes. *Australian Journal of Earth Sciences* **59**, 983–1005.

Tsuchiyama, A. (1985). Dissolution kinetics of plagioclase in the melt of the system diopside-albite-anorthite, and origin of dusty plagioclase in andesites. *Contributions to Mineralogy and Petrology* **89**, 1–16.

Ubide, T., Caulfield, J., Brandt, C., Bussweiler, Y., Mollo, S., Di Stefano, F., Nazzari, M. & Scarlato, P. (2019b). Deep magma storage revealed by multi-method elemental mapping of Clinopyroxene Megacrysts at Stromboli Volcano. *Frontiers in Earth Science* **7**.

Ubide, T., Gale, C., Larrea, P., Arranz, E., Lago, M. & Tierz, P. (2014). The relevance of crystal transfer to magma mixing: a case study in composite dykes from the Central Pyrenees. *Journal of Petrology* **55**, 1535–1559.

Ubide, T. & Kamber, B. S. (2018). Volcanic crystals as time capsules of eruption history. *Nature Communications* **9**, 326.

Ubide, T., McKenna, C. A., Chew, D. M. & Kamber, B. S. (2015). High-resolution LA-ICP-MS trace element mapping of igneous minerals: in search of magma histories. *Chemical Geology* **409**, 157–168.

Ubide, T., Mollo, S., Zhao, J.-X., Nazzari, M. & Scarlato, P. (2019a). Sector-zoned clinopyroxene as a recorder of magma history, eruption triggers, and ascent rates. *Geochimica et Cosmochimica Acta* **251**, 265–283.

Ubide, T., Neave, D. A., Petrelli, M. & Longpré, M. A. (2021). Editorial: crystal archives of magmatic processes. *Frontiers in Earth Science* **9**.

Ubide, T., Larrea, P., Becerril, L. & Galé, C. (2022). Volcanic plumbing filters on ocean- island basalt geochemistry. *Geology* **50**, 26–31.

Van Gerve, T. D., Neave, D. A., Almeev, R., Holtz, F. & Namur, O. (2020). Zoned crystal records of transcrustal magma transport, storage and differentiation: insights from the Shatsky rise oceanic plateau. *Journal of Petrology* **61**, 080.

Vasconcelos, P. M., Knesel, K. M., Cohen, B. E. & Heim, J. A. (2008). Geochronology of the Australian Cenozoic: a history of tectonic and igneous activity, weathering, erosion, and sedimentation. *Australian Journal of Earth Sciences* **55**, 865–914.

Vasconcelos, P. M., Onoe, A. T., Kawashita, K., Soares, A. J. & Teixeira, W. (2002). $^{40}Ar/^{39}Ar$ geochronology at the Instituto de Geociências, USP: instrumentation, analytical procedures, and calibration. *Anais da Academia Brasileira de Ciências* **74**, 297–342.

Viccaro, M., Garozzo, I., Cannata, A., Di Grazia, G. & Gresta, S. (2014). Gas burst vs. gas-rich magma recharge: a multidisciplinary study to reveal factors controlling triggering of the recent paroxysmal eruptions at Mt. Etna. *Journal of Volcanology and Geothermal Research* **278-279**, 1–13.

Viccaro, M., Giacomoni, P. P., Ferlito, C. & Cristofolini, R. (2010). Dynamics of magma supply at Mt. Etna volcano (southern Italy) as revealed by textural and compositional features of plagioclase phenocrysts. *Lithos* **116**, 77–91.

Villaseca, C., García Serrano, J. & Orejana, D. (2020). Pyroxenites and Megacrysts from alkaline melts of the Calatrava volcanic field (Central Spain): inferences from trace element geochemistry and Sr-nd isotope composition. *Frontiers in Earth Science* **8**, 132.

Wanke, M., Clynne, M. A., von Quadt, A., Vennemann, T. W. & Bachmann, O. (2019). Geochemical and petrological diversity of mafic magmas from Mount St. Helens. *Contributions to Mineralogy and Petrology* **174**, 10.

Wass, S. Y. (1979). Multiple origins of clinopyroxenes in alkali basaltic rocks. *Lithos* **12**, 115–132.

Waters, L. E. & Lange, R. A. (2016). No effect of H2O degassing on the oxidation state of magmatic liquids. *Earth and Planetary Science Letters* **447**, 48–59.

Waltenberg, K. (2006) 40Ar/39Ar geochronology of lava flows at Carnarvon Gorge, Buckland Volcano. Honours, University of Queensland, Brisbane (unpubl.).

Wellman, P. (1971) The age and palaeomagnetism of the Australian Cenozoic volcanic rocks (unpubl.).

Wellman, P. & McDougall, I. (1974a). Potassium-argon ages on the Cainozoic volcanic rocks of New South Wales. *Journal Ofthe Geological Society of Australia* **21**, 247–272.

Wellman, P. & McDougall, I. (1974b). Cainozoic igneous activity in eastern Australia. *Tectonophysics* **23**, 49–65.

Wellman, P., McElhinny, M. W. & McDougall, I. (1969). On the polar-wander path for Australia during the Cenozoic. *Geophysical Journal International* **18**, 371–395.